THE ASTROPHYSICAL JOURNAL, 397:88–116, 1992 September 20

FIRST-ORDER FERMI ACCELERATION IN SPHERICALLY SYMMETRIC FLOWS: SOLUTIONS INCLUDING QUADRATIC LOSSES

PETER A. BECKER[1]
E. O. Hulburt Center for Space Research, Code 4121.11, Naval Research Laboratory, Washington, DC 20375-5000
Received 1992 January 30; accepted 1992 March 24

ABSTRACT

We obtain a new, exact solution for the Green's function describing the transport of relativistic particles in steady, spherically symmetric background flows, including the effects of first-order Fermi acceleration, spatial diffusion, bulk advection, and losses proportional to the square of the particle momentum. The flow velocity of the background (scattering) plasma and the spatial diffusion coefficient are assumed to vary as $v(r) \propto r^{-\alpha}$ and $\kappa(p, r) \propto r^{\beta} K(p)$, respectively, where r is the radius and $K(p)$ is an arbitrary function of the particle momentum p. The momentum loss rate is assumed to vary quadratically with the particle momentum as $\langle \dot{p} \rangle_{\rm loss} = Ap^2 v/r$, where A = constant. Examples of quadratic loss mechanisms include synchrotron and inverse Compton; in the synchrotron case, the implied magnetic field variation is $B^2 \propto v/r$, which may be satisfied in galaxy cluster cooling flows. Losses exactly balance first-order Fermi acceleration at the critical momentum $p_c = (2 - \alpha)/(3A)$, which is a single constant for the entire flow if A = constant. Finite losses cause a compression of the dynamic range of the momentum variable relative to the lossless case ($A = 0$), since particles injected with momentum p_0 are confined to the interval (p_0, p_c). The sign of v is unrestricted, and therefore our model can be used to study the transport of relativistic particles in both winds and accretion flows.

Previous studies of particle transport in radio sources have considered the effects of spatial diffusion and synchrotron losses on relativistic electrons propagating through static background plasmas. The inclusion of bulk motions of the plasma affects both the energization of the electrons (via Fermi acceleration) and the spatial transport (via advection). In accretion flows, advection tends to drag the electrons inward, reducing the number escaping from the flow, while Fermi acceleration tends to increase the energy of the electrons that do escape. We find that the spectrum of electrons at large radii (and hence the associated synchrotron emission) is significantly harder in the presence of bulk motions, and that extended, power-law radio spectra are a natural consequence of either monoenergetic or power-law electron injection. In particular, we conclude that Fermi acceleration may help to explain the production of core-halo radio emission in cooling flows. Therefore core halos may provide independent evidence for dynamical cooling processes in clusters of galaxies.

It has been previously pointed out that the flux of relativistic particles emerging from an accretion flow vanishes for certain values of the parameters (α, β, γ) when $K(p) \propto p^{\gamma}$. This region of the parameter space is consequently unobservable if the relativistic particles are photons. However, if the relativistic particles are electrons, we show that observable power-law radio emission can be produced even when the emergent flux of *electrons* vanishes.

Subject headings: acceleration of particles — galaxies: cooling flows — methods: analytical — plasmas — radio sources: extended — relativity

1. INTRODUCTION

The transport of relativistic particles plays a central role in the production of observable radiation in a variety of astrophysical environments, including supernova remnants, accretion flows around black holes and neutron stars, and the Galaxy as a whole. Our interest in the problem of particle transport in dynamic media has been motivated by observations of amorphous "halo" radio emission in clusters of galaxies, on scales ranging from hundreds to thousands of kiloparsecs (Hanisch 1982). Large radio halos with diameters ~ 1 Mpc comparable to the size of the entire cluster have been observed in Coma and in other relaxed clusters without X-ray dominant galaxies (Vestrand 1982). Smaller-scale radio *core halos* with diameters ~ 100 kpc have been observed surrounding the central dominant galaxies in several cooling-flow clusters, including Perseus (Gisler & Miley 1979) and M87/Virgo (Hanisch & Erickson 1980). If the relativistic electrons responsible for the extended radio emission diffuse from active galaxies located near the cluster centers, then *in situ* acceleration seems to be required in order to offset synchrotron losses and thereby explain the sizes of the large, Coma-class halos (Jaffe 1977), unless super-Alfvénic transport is invoked. Various attempts to devise alternative transport schemes have met with limited success (Hanisch 1982). However, the synchrotron lifetime does not constrain the propagation velocity as severely in core halos, which are an order of magnitude smaller in size.

While most of the theoretical effort has focused on the production of Coma-class halos, it has become apparent in recent years that cooling-flow core halos actually comprise a much larger observational class, possibly also including the diffuse radio structures seen in isolated elliptical galaxies (Burns 1990; Fabian et al. 1986). If the radio emission in these cases is related to the presence of bulk motions, then the potential exists for establishing an important connection between the X-ray and radio emitting plasmas in clusters and isolated ellipticals containing cooling flows.

[1] NRC-NRL Cooperative Research Associate.

There have been previous suggestions in the literature regarding possible connections between cooling flows and core-halo radio emission. Soker & Sarazin (1990) suggested that compression in cooling flows may amplify the intracluster magnetic field to the point of reconnection, hence providing a source of relativistic particles for the radio halo. Begelman (1986) has pointed out that cooling flows may feed black holes in the cores of central dominant galaxies, fueling enhanced nuclear activity. Burns (1990) suggested that the increased pressure in the intracluster medium due to the presence of the cooling flow may reduce expansional losses.

There may be other effects more directly related to the dynamical nature of the cooling flow. Relativistic electrons expelled from the central active galaxy will collide with irregularities and waves in the magnetic field as the electrons propagate outward through the intracluster gas. If the field is sufficiently tangled and "frozen" into the cooling gas flowing toward the cluster center, then the collisions will have two important consequences. First, energy will be transferred from the background (cooling) flow to the relativistic electrons via first-order Fermi acceleration due to the average (bulk) motion of the scattering centers. Second, the inflowing background plasma will tend to "drag" the electrons toward the center of the cluster, reducing the density of electrons at large radii. These effects will combine to produce observable modifications in both the spatial and energetic distributions of the relativistic electrons powering the extended radio emission.

The importance of first-order Fermi acceleration depends sensitively on the configuration of the intracluster magnetic field. Magnetic fields of the required (tangled) topology are actually implied by the existence of the cooling flows, which depend upon disordered fields to suppress thermal conduction (Sarazin 1986). This is verified by observations of the rotation measure in clusters (Hennessy, Owen, & Eilek 1989; Soker & Sarazin 1990), and by theoretical models for intracluster turbulence (De Young 1980; Jaffe 1980; Roland 1981).

The electrons also experience *second-order* Fermi acceleration due to the random motions of the scattering centers with respect to the background flow. By augmenting the particle acceleration rate, the second-order Fermi process extends the particle spectrum to energies beyond the cutoff obtained by balancing synchrotron losses against first-order Fermi acceleration. Since the Alfvén velocity is thought to exceed the flow velocity in cooling flows, second-order Fermi acceleration is likely to play a role comparable to first-order Fermi acceleration in producing core-halo radio emission. However, in this paper we are primarily concerned with the direct effects of cooling-flow dynamics on the transport and acceleration of relativistic electrons. Hence we neglect second-order Fermi acceleration here, and defer further consideration of this process to future studies. We simply note that by focusing on the first-order effect, we are *underestimating* the average acceleration rate for particles of a given energy.

In this paper we analyze the transport of relativistic particles in spherically symmetric, steady state accretion flows and winds, including the effects of first-order Fermi acceleration, spatial diffusion, bulk advection, and losses proportional to the square of the particle momentum. The results of previous studies focusing on the effects of linear loss terms cannot be applied to relativistic electrons, which cool primarily via quadratic loss mechanisms such as synchrotron and inverse-Compton emission. In § 2, we derive an exact expression for the Green's function corresponding to the continual injection of monoenergetic particles from a source at an arbitrary radius. Our results are compared with those of Cowsik & Lee (1982), Webb & Bogdan (1987), and Schneider & Bogdan (1989). In § 3, the behavior of this solution is examined in detail for the special case of momentum-independent diffusion, and closed-form expressions are obtained for the relativistic particle number, energy, and loss-power densities, and for the distribution function corresponding to the continual injection of particles with a power-law spread in momentum. In § 4 we calculate the corresponding self-consistent synchrotron emissivity for monoenergetic and power-law electron injection in cooling flows. The analysis in § 2 permits the diffusion coefficient to assume an arbitrary (separable) momentum dependence, although for simplicity the results quoted in §§ 3 and 4 are confined to the case of momentum-independent diffusion. In § 5 we conclude with a summary of the main results and a discussion of amorphous radio emission in clusters of galaxies.

2. BASIC EQUATIONS AND SOLUTIONS

The theory of particle transport in spherically symmetric media is a primary component in studies of the energization of particles in astrophysical winds and accretion flows. Most such studies are based on the fundamental Fokker-Planck equation describing the effects of first-order Fermi acceleration, spatial diffusion, and bulk advection, derived by Parker (1965), Gleeson & Axford (1967), and Skilling (1975). For a review of the subject, see Gleeson & Webb (1980). Cowsik & Lee (1982) obtained exact solutions to the Fokker-Planck equation describing the transport of monoenergetic particles injected at a stationary stand-off shock in a spherical accretion flow with a momentum-independent diffusion coefficient. Webb & Bogdan (1987) extended the results of Cowsik and Lee by adding a collisional loss term proportional to both the particle momentum and the divergence of the bulk flow velocity. The diffusion coefficient employed by Cowsik & Lee (1982) and Webb & Bogdan (1987) vanishes downstream from the shock, and equals the product of the bulk flow velocity and the radius in the upstream region. The corresponding diffusion velocity equals either zero ($r < r_{\rm shock}$) or the bulk flow velocity ($r > r_{\rm shock}$). Unfortunately, this prescription for the diffusion coefficient precludes the interesting physical effects associated with finite but unequal diffusion and bulk flow velocities.

Schneider & Bogdan (1989) remedied this shortcoming by allowing the diffusion coefficient to vary as a power law in radius and particle momentum. The momentum loss term appearing in the transport equation studied by Webb & Bogdan (1987) and Schneider & Bogdan (1989) is directly proportional to the particle momentum, and therefore provides an apt description of the losses suffered by cosmic-ray protons due to nuclear collisions with a freely falling background plasma. However, relativistic electrons lose energy primarily via synchrotron and inverse Compton emission, with a rate proportional to the *square* of the particle momentum. Here we examine the consequences of replacing the linear-loss term studied previously with a quadratic dependence, relevant for the transport of relativistic electrons. In this section we obtain the Green's function for monoenergetic particle injection in a spherically symmetric wind or accretion flow, including first-order Fermi acceleration, spatial diffusion, bulk advection, and losses proportional to the square of the particle momentum. Our analysis can accommodate any separable diffusion coefficient with

a power-law radial dependence and essentially represents the quadratic analog to the linear-loss theory developed by Schneider & Bogdan (1989).

2.1. *Transport Equation*

The time-dependent transport equation governing the evolution of the isotropic particle distribution function f is (Gleeson & Axford 1967; Skilling 1975)

$$\frac{\partial f}{\partial t} + \nabla \cdot F - \frac{1}{p^2}\frac{\partial}{\partial p}\left(p^2 D \frac{\partial f}{\partial p}\right) + \frac{1}{p^2}\frac{\partial}{\partial p}\left(p^2 \langle \dot{p} \rangle_{\rm loss} f\right) = -\frac{1}{3p^2}\frac{\partial}{\partial p}\left(p^3 v \cdot \nabla f\right) + \dot{f}\,, \tag{2.1}$$

where the specific (spatial) particle flux F is given by

$$F(p, r) = -\kappa \frac{\partial f}{\partial r} - \frac{vp}{3}\frac{\partial f}{\partial p}\,, \tag{2.2}$$

and the quantities f, p, κ, D, v, $\langle \dot{p} \rangle_{\rm loss}$, and $\dot{f}$ denote the phase-space density of particles, the particle momentum, the spatial diffusion coefficient, the momentum diffusion coefficient, the radial velocity of the background plasma, the momentum loss rate, and the particle source distribution, respectively. The first term on the right-hand side of equation (2.1) expresses the differential work performed on the relativistic particles by the background flow (Gleeson & Webb 1978; Cowsik & Lee 1982). The momentum diffusion coefficient D describes the effect of second-order (statistical) acceleration due to random motions of the scattering centers with respect to the background flow. If for example the particles are relativistic electrons resonantly scattered by Alfvén waves propagating along the local magnetic field in both directions, then D and κ are related by (Skilling 1975; Schlickeiser 1989a, b)

$$D(p, r)\kappa(p, r) = c_0 v_{\rm A}^2 p^2\,, \tag{2.3}$$

where $v_{\rm A}$ is the Alfvén velocity and c_0 is a dimensionless constant of order unity that depends on the power spectrum of the Alfvén waves. Equation (2.3) can be applied in a much broader context by simply replacing $v_{\rm A}^2$ with the mean-square velocity of the scattering centers. The total number density of relativistic particles n is given in terms of the distribution function f by

$$n = \int_0^\infty 4\pi p^2 f\, dp \qquad (\propto {\rm cm}^{-3})\,. \tag{2.4}$$

If the relativistic particles are photons instead of massive particles, then $f = 2\bar{n}/h^3$, where $\bar{n}$ is the photon occupation number and h is Planck's constant.

We shall assume that the bulk flow velocity v, the diffusion coefficient κ, the particle source term $\dot{f}$, and the momentum loss rate $\langle \dot{p} \rangle_{\rm loss}$ are all time-independent, and solve for the steady state particle distribution $f(p, r)$ corresponding to the continual injection of particles with momentum p_0 at radius r_0. The source term describing this situation is

$$\dot{f}(p, r) = \frac{\dot{N}_0}{(4\pi r_0 p_0)^2}\,\delta(p - p_0)\delta(r - r_0)\,, \tag{2.5}$$

which corresponds to a total particle injection rate $\dot{N}_0$ (s^{-1}) according to the normalization introduced in equation (2.4). Neglecting momentum diffusion ($D = 0$), equations (2.1), (2.2), and (2.5) can be combined with the assumption of spherical symmetry to obtain the steady state transport equation

$$v\frac{\partial f}{\partial r} - \frac{1}{3r^2}\frac{d}{dr}(r^2 v)p\frac{\partial f}{\partial p} + \frac{1}{p^2}\frac{\partial}{\partial p}\left(p^2 \langle \dot{p} \rangle_{\rm loss} f\right) - \frac{1}{r^2}\frac{\partial}{\partial r}\left(r^2 \kappa \frac{\partial f}{\partial r}\right) = \frac{\dot{N}_0}{(4\pi r_0 p_0)^2}\,\delta(p - p_0)\delta(r - r_0)\,, \tag{2.6}$$

where the terms from left to right represent the comoving (convective) time derivative, first-order Fermi acceleration (or deceleration) due to the motion of the scattering centers, momentum losses, spatial diffusion, and monoenergetic particle injection, respectively. We shall assume that the background flow velocity v and the spatial diffusion coefficient κ satisfy the relations

$$v(r) = v_0\left(\frac{r}{r_0}\right)^{-\alpha}\,, \qquad \alpha < 2\,, \tag{2.7}$$

$$\kappa(p, r) = K(p)\left(\frac{r}{r_0}\right)^{\beta}\,, \tag{2.8}$$

where α, β, and v_0 are constants. The unspecified function $K(p)$ describes the momentum dependence of the diffusion coefficient, and the restriction on α ensures that the density of the background plasma decreases with increasing radius. Since the sign of v_0 is unrestricted, the background flow can take the form of either an accretion or a wind.

2.2. *Fermi Acceleration versus Quadratic Losses*

Relativistic electrons in clusters of galaxies cool by emitting synchrotron and inverse-Compton radiation. If the distribution function is isotropic, then electrons with momentum p lose momentum via synchrotron at the average rate (e.g., Rybicki & Lightman 1979)

$$\langle \dot{p} \rangle_{\rm synch} = -AB^2 p^2\,, \tag{2.9a}$$

where

$$A = \frac{4e^4}{9m_e^4 c^6}, \tag{2.9b}$$

and B, c, m_e, and e denote the magnetic field strength, the speed of light, and the electron rest mass and charge, respectively. The rate at which electrons lose momentum via inverse-Compton scattering soft background radiation is related to $\langle \dot{p} \rangle_{\rm synch}$ by

$$\langle \dot{p} \rangle_{\rm Compt} = \frac{U_{\rm ph}}{U_B} \langle \dot{p} \rangle_{\rm synch}, \tag{2.10}$$

where $U_B = B^2/(8\pi)$ is the magnetic energy density and $U_{\rm ph}$ is the energy density of the background radiation. Since the synchrotron and inverse-Compton loss rates both vary as the square of the particle momentum, each process can be modeled as a special case of the general quadratic loss rate

$$\langle \dot{p} \rangle_{\rm loss}(p, r) = -R(r)p^2, \tag{2.11a}$$

where

$$R(r) = \begin{cases} AB^2, & \text{synchrotron}, \\ 8\pi A U_{\rm ph}, & \text{inverse Compton}, \end{cases} \tag{2.11b}$$

expresses the spatial dependence of the losses.

The first-order Fermi acceleration rate for particles colliding with scattering centers undergoing bulk motion is (Jokipii 1971; Gleeson & Webb 1978)

$$\langle \dot{p} \rangle_{\rm Fermi} = -(\nabla \cdot v)\frac{p}{3}, \tag{2.12}$$

and consequently the net acceleration rate $\langle \dot{p} \rangle_{\rm net} \equiv \langle \dot{p} \rangle_{\rm Fermi} + \langle \dot{p} \rangle_{\rm loss}$ vanishes for particles with momentum $p = p_c$, where

$$p_c \equiv \frac{-\nabla \cdot v}{3R(r)} \tag{2.13}$$

is a function of radius in general. The net acceleration rate $\langle \dot{p} \rangle_{\rm net}$ changes sign at $p = p_c$, with $\langle \dot{p} \rangle_{\rm net} > 0$ for $p < p_c$; hence p_c represents the (local) critical momentum, toward which the particles are continually driven under the combined influence of Fermi acceleration and quadratic losses. Note that the Fermi acceleration rate and the critical momentum are both formally negative if the divergence of the flow velocity is positive.

We seek the solution to the transport equation (2.6) with the flow velocity and the diffusion coefficient given by equations (2.7) and (2.8), respectively, and the momentum loss rate $\langle \dot{p} \rangle_{\rm loss}$ given by equation (2.11). The mathematical approach to solution of the transport equation is simplified substantially if the spatial dependence of the loss rate (and hence B^2 and $U_{\rm ph}$) satisfies

$$R(r) = R_0\left(\frac{r}{r_0}\right)^{-1-\alpha} \propto \frac{v}{r}, \tag{2.14}$$

where R_0 is a positive constant, since then the critical momentum

$$p_c = \frac{-v_0(2-\alpha)}{3R_0 r_0}, \qquad \alpha < 2 \tag{2.15}$$

is a single constant for the entire flow, and $\langle \dot{p} \rangle_{\rm loss} \propto p^2 r^{-1-\alpha}$. The corresponding case $\langle \dot{p} \rangle_{\rm loss} \propto p r^{-1-\alpha}$ has been studied in detail by Webb & Bogdan (1987) and Schneider & Bogdan (1989) in the context of cosmic-ray acceleration.

The variation of the magnetic field strength implied by equation (2.14) for the case of synchrotron losses, $B^2 \propto v/r$, is not consistent with the usual result $B \propto r^{-2}$ for the variation of the radial component of a spherically symmetric, force-free field. However, theoretical models for cooling flows that include turbulent amplification of the small-scale component of the magnetic field predict $B \propto v \propto r^{-1}$ (Soker & Sarazin 1990; White & Sarazin 1987), which is consistent with equation (2.14). We shall assume that equation (2.14) is satisfied, and therefore that particles are driven toward the critical momentum p_c everywhere in the flow with a net rate

$$\langle \dot{p} \rangle_{\rm net} = \frac{-v_0(2-\alpha)}{3r_0}\left(\frac{r}{r_0}\right)^{-1-\alpha} p\left(1 - \frac{p}{p_c}\right) \tag{2.16}$$

that depends upon both radius and momentum. This effectively compresses the dynamic range of the momentum variable, since particles injected with momentum p_0 are subsequently confined to the interval (p_0, p_c). The restriction on α (eq. [2.7]) implies that p_c is positive for an inflow ($v_0 < 0$) and formally negative for an outflow. In the outflow case, the particles are actually confined to the restricted interval $(0, p_0)$, corresponding to the physically allowed values of the momentum.

When p_c = constant, the transport equation for the relativistic electrons can be expressed in terms of the *dimensionless momentum*

$$\psi \equiv \frac{p}{m_e c}, \qquad \psi_c \equiv \frac{p_c}{m_e c} = \frac{-v_0(2-\alpha)}{3m_e c R_0 r_0}, \tag{2.17}$$

as

$$\psi\left(1-\frac{\psi}{\psi_c}\right)\frac{\partial g}{\partial \psi} - \left(\frac{3r}{2-\alpha}\right)\frac{\partial g}{\partial r} = -\left(\frac{3}{2-\alpha}\right)\frac{r^{1+\alpha}}{r_0^{\alpha} v_0}\left[\frac{K(\psi)}{r_0^{\beta} r^2}\frac{\partial}{\partial r}\left(r^{2+\beta}\frac{\partial g}{\partial r}\right) + \dot{g}\right], \tag{2.18}$$

where

$$g(\psi, r) \equiv \left(1-\frac{\psi}{\psi_c}\right)^4 f(\psi, r), \qquad \dot{g}(\psi, r) \equiv \left(1-\frac{\psi}{\psi_c}\right)^4 \dot{f}(\psi, r), \tag{2.19}$$

and $\dot{f}$ is given by equation (2.5). The dimensionless momentum $\psi = \sqrt{\gamma_L^2 - 1}$, where γ_L is the electron Lorentz factor. For the highly relativisticelectrons treated here, $\psi \approx \gamma_L \gg 1$, and we shall therefore refer to ψ as the Lorentz factor throughout the remainder of the paper. In the limit $|\psi_c| \to \infty$ (no losses), equation (2.18) also models the acceleration of photons with frequency $\nu = \psi m_e c^2/h$.

2.3. *Adiabatic Invariance*

The left-hand side of equation (2.18) is proportional to the total derivative of g with respect to ψ evaluated along the characteristic trajectory in (ψ, r) space defined by the relation

$$\left(\frac{\partial g}{\partial \psi}\right)_y \equiv \left(\frac{\partial g}{\partial \psi}\right)_r + \left(\frac{\partial g}{\partial r}\right)_{\psi}\left(\frac{\partial r}{\partial \psi}\right)_y, \tag{2.20}$$

where each value of the generalized "adiabatic invariant" $y \equiv y(\psi, r)$ corresponds to a unique trajectory. We can obtain an expression for y by comparing the left-hand side of equation (2.18) with equation (2.20). Integration yields

$$y(\psi, r) \equiv \left(\frac{r}{r_0}\right)^{2-\alpha}\left|\frac{1}{\psi} - \frac{1}{\psi_c}\right|^{-3}, \tag{2.21}$$

where the integration constant has been suitably chosen. In the zero diffusion limit ($\kappa \to 0$), the distribution g approaches an exact function of y alone, and the momentum of a particle evolves according to

$$\rho\left(\frac{1}{p} - \frac{1}{p_c}\right)^3 = \text{constant}, \tag{2.22}$$

where $\rho \propto r^{-2}v^{-1}$ is the mass density of the background plasma.[2] In the case of negligible losses ($|\psi_c| \to \infty$), equation (2.21) for y reduces to the standard adiabatic relation

$$y \propto \frac{p^3}{\rho}. \tag{2.23}$$

2.4. *Solutions*

In terms of y (eq. [2.21]) and the new momentum variable

$$x(\psi) \equiv \left|\frac{3(2-\alpha)}{r_0 v_0}\int_{\psi_0}^{\psi} \psi_*^{-2} K(\psi_*)\left(\frac{1}{\psi_*} - \frac{1}{\psi_c}\right)^{-3\eta-1} d\psi_*\right|, \tag{2.24}$$

where

$$\psi_0 \equiv \frac{p_0}{m_e c} \tag{2.25}$$

is the Lorentz factor of the injected electrons, the transport equation (2.18) reduces to the classic diffusion equation (e.g., Webb 1982)

$$\frac{\partial g}{\partial x} = \frac{\partial}{\partial y}\left(y^{2-\eta}\frac{\partial g}{\partial y}\right) + \frac{3\dot{N}_0}{(4\pi r_0)^2 m_e^3 c^3 |v_0|}\delta(y - y_0)\delta(x), \tag{2.26}$$

where

$$\eta \equiv \frac{1-\alpha-\beta}{2-\alpha}, \tag{2.27}$$

[2] Provided the mass transport rate for the background plasma, $\dot{M} \equiv 4\pi r^2 \rho v$, is independent of radius; this may be violated in cooling flows.

and

$$y_0 \equiv \left| \frac{1}{\psi_0} - \frac{1}{\psi_c} \right|^{-3} . \tag{2.28}$$

Here x plays the same role as the time t in the parabolic heat diffusion equation $\partial f/\partial t = \nabla^2 f$.

Equation (2.26) can be solved using Laplace transform techniques as detailed in the Appendix. The result (eq. [A17]) can be combined with equation (2.19) to obtain the Green's function solution

$$f_G(\psi, r) = \frac{3\dot{N}_0(1 - \psi/\psi_c)^{-4}}{(4\pi r_0)^2 m_e^3 c^3 |v_0|} \frac{(yy_0)^{(\eta-1)/2}}{|\eta| x} \exp\left[-\left(\frac{y_0^\eta + y^\eta}{\eta^2 x} \right) \right] I_\mu \left[\frac{2(yy_0)^{\eta/2}}{\eta^2 x} \right] , \tag{2.29}$$

where I_μ is the modified Bessel function of the first kind (Abramowitz & Stegun 1970), and

$$\mu \equiv 1 - \frac{1}{\eta} . \tag{2.30}$$

Equation (2.29) is our main result, and most of the remainder of the paper is devoted to analyzing its properties.

The Green's function f_G gives the response to the continual injection of monoenergetic particles into a wind or accretion flow with bulk velocity $v \propto r^{-\alpha}$ and diffusion coefficient $\kappa \propto r^\beta K(p)$, where α and β are arbitrary constants and K is an arbitrary function. The behavior of the solution is therefore quite rich, and several distinct modes of particle transport are possible. The important new aspects of this solution center on the inclusion of quadratic losses due to synchrotron or inverse-Compton emission. In order to incorporate this additional effect without undue mathematical complexity, we have assumed that the magnetic field and the soft photon energy density vary as $B^2 \propto U_{ph} \propto v/r$ (eq. [2.14]). This choice has the advantage of making the critical momentum p_c (eq. [2.15]) a constant for the entire flow, but it also significantly limits the range of applicability of the results. Here we give examples of wind and accretion scenarios that can be treated using our formalism.

In a typical accretion scenario, relativistic electrons experience first-order Fermi acceleration due to collisions with scattering centers inflowing with radial velocity $v \propto r^{-1}$. The electrons also cool due to some combination of (i) synchrotron emission in a magnetic field with strength $B \propto r^{-1}$, and (ii) inverse-Compton scattering of soft photons with energy density $U_{ph} \propto r^{-2}$. The momentum loss rate in either case is $\langle \dot{p} \rangle_{loss}(p, r) \propto (p/r)^2$. Theoretical models for galaxy cluster cooling flows in which the small-scale magnetic field is amplified by strong turbulence predict $B \propto v \propto r^{-1}$ (Soker & Sarazin 1990; White & Sarazin 1987), which is consistent with scenario (i). The synchrotron radio spectrum for this case is calculated in § 4, and the production of core-halo radio emission in cooling flows is discussed in § 5.

In a typical wind scenario, relativistic electrons cool due to collisions with scattering centers outflowing with radial velocity $v \propto r$, and suffer additional losses due to some combination of (iii) synchrotron emission in a magnetic field of constant strength, and (iv) inverse-Compton scattering of soft photons with a constant incident energy density. The loss rate in either of these cases is $\langle \dot{p} \rangle_{loss}(p, r) \propto p^2$. Scenario (iv) may describe the transport of relativistic electrons in winds from active galaxies when the radiative losses are primarily due to inverse-Compton scattering of cosmic background photons.

2.5. *Asymptotic Behavior*

We have shown that particles injected with momentum p_0 are subsequently confined to the interval (p_0, p_c) when the momentum loss rate satisfies equation (2.14). Recall that if the plasma is outflowing ($v > 0$) and $\alpha < 2$, then p_c is formally negative according to equation (2.15), and therefore the physically allowed values of the momentum actually lie in the restricted range $(0, p_0)$. Hence the distribution function can extend to infinite momentum only if $p_c \to \infty$, which corresponds to inflow with negligible losses. It is of interest to examine the behavior of the Green's function as $p \to \infty$ in this case, and in particular to establish the conditions favoring the development of a high-energy power-law tail in the particle distribution. In order to quantify the asymptotic behavior of the distribution, we must specify the function $K(p)$ which expresses the momentum dependence of the spatial diffusion coefficient κ (eq. [2.8]). The power-law dependence $K(p) = K_0(p/m_e c)^\gamma$ with K_0 and γ constants is of particular interest, since it describes the diffusion of electrons due to resonant interactions with Alfvén waves propagating in the local magnetic field (e.g., Eilek 1984). In this case, equation (2.29) can be combined with equations (9.6.7) and (9.7.1) of Abramowitz & Stegun (1970) to obtain

$$\Gamma_\infty \equiv \lim_{p \to \infty} \left(\frac{\partial \ln f_G}{\partial \ln p} \right) = \begin{cases} 3\eta - 3 , & \eta \le 0, \gamma + 3\eta < 0 , \\ -3\eta - \gamma\left(2 - \dfrac{1}{\eta}\right) , & \gamma \ge 0, \gamma + 3\eta > 0 , \\ -\infty , & \gamma < 0, \eta > 0 , \end{cases} \tag{2.31}$$

for the case of inflow with negligible losses. These results are indicated graphically in Figure 1.

Schneider & Bogdan (1989) recognized the existence of asymptotic power-law solutions for the case $\eta < 0$. However, we point out (apparently for the first time) that asymptotic power laws can also occur when $\eta > 0$ and $\gamma \ge 0$ in the absence of losses. In fact, exponential cutoffs in the particle spectrum are confined to the lower-right quadrant ($\eta > 0$, $\gamma < 0$) of the parameter space depicted in Figure 1, due to a unique combination of circumstances. Relativistic particles injected into an accretion flow gain momentum due to first-order Fermi acceleration at the rate $\langle \dot{p} \rangle_{Fermi} = -(\nabla \cdot v)(p/3)$ for as long as they reside in the flow. This rate varies with radius and particle momentum, but is independent of the spatial diffusion coefficient. As we discuss in § 3, the transport of particles for solutions in the ($\eta > 0$, $\gamma < 0$) quadrant is dominated by inward-bound advection for large radii and for large particle momenta.

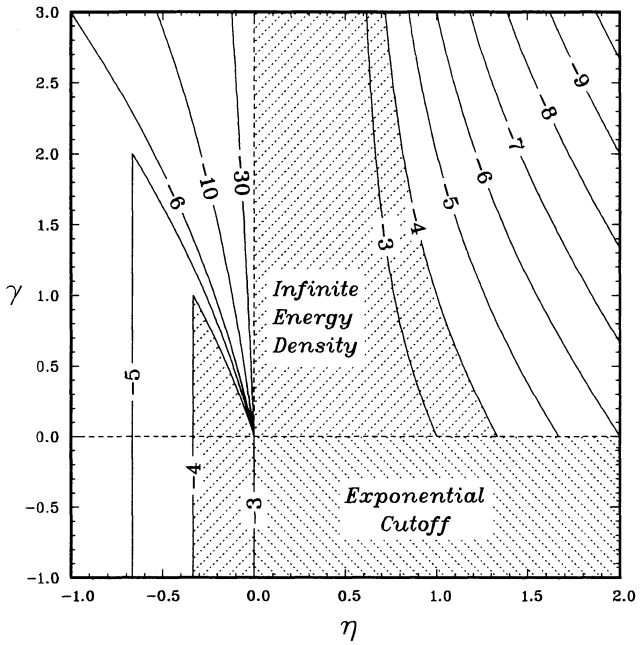

FIG. 1.—Contour plot of the asymptotic spectral index Γ_∞ (eq. [2.31]) as a function of η (eq. [2.27]) and γ [where $K(p) \propto p^\gamma$; see eq. (2.8)] for cases involving inflow with negligible losses.

Hence particles accelerating and diffusing outward through the flow experience a rapidly decreasing diffusion coefficient, and soon become entrained by the inflowing background plasma. Consequently most of the particles are rapidly swept into the sink at the center of the flow, with residence times too short to establish a high-energy power-law tail.[3]

2.6. *Trapping Radius*

When the background flow velocity exceeds the local diffusion velocity, the particles are "trapped" within the flow, and spatial transport is accomplished primarily by advection (Begelman 1979). The transition between advection-dominated and diffusion-dominated behavior takes place at the "trapping radius," $r = r_t$, which is a function of the particle momentum if the diffusion coefficient has a momentum dependence. The trapping radius concept has been used to study radiative transfer in hot accreting gas (Begelman 1979) and in hot winds (Becker & Begelman 1986). In these fully ionized, nonrelativistic flows, Thomson scattering provides the dominant opacity, and since the Thomson cross section is independent of the photon momentum, the trapping radius is the same for all photons. However, in cases involving the transport of relativistic electrons, the scattering cross section is usually a function of the electron momentum, and therefore we shall assume that the diffusion coefficient is given by equation (2.8) with $K(p)$ unrestricted.

The specific particle flux measured by an observer moving outward with velocity $v_{\rm obs}$ at radius r is (eq. [2.2])

$$F(p, r) = -\frac{1}{3}(v - v_{\rm obs})p\frac{\partial f}{\partial p} - \kappa\frac{\partial f}{\partial r}, \tag{2.32}$$

where the terms on the right-hand side represent the fluxes sweeping past the observer due to the advection of particles by the background flow and the diffusion of particles relative to the flow, respectively. Hence in the rest frame of an observer comoving with the background plasma ($v_{\rm obs} = v$), the spatial transport is entirely due to diffusion, with specific particle flux

$$F_{\rm diff}(p, r) \equiv -\kappa\frac{\partial f}{\partial r}. \tag{2.33}$$

The specific diffusion velocity

$$v_{\rm diff}(p, r) \equiv -\kappa\frac{\partial \ln f}{\partial r} \tag{2.34}$$

is defined as the average radial velocity of particles with momentum p and radius r, measured in the comoving frame. It is interesting to note that $v_{\rm diff}(p, r)$ is not in general equal to the average *drift* velocity of particles relative to the background plasma. To

[3] It should be noted that momentum diffusion (statistical acceleration), which has been neglected here, causes asymptotic power-laws to decay for all values of (η, γ), even in the absence of losses (Cowsik 1986; Lerche & Schlickeiser 1988).

demonstrate this, we rewrite the transport equation (2.1) for the case of pure diffusion as

$$\left(\frac{\partial f}{\partial t}\right)_{\rm diff} = \frac{K(p)}{r_0^{\beta} r^2}\frac{\partial}{\partial r}\left[\frac{\partial}{\partial r}(r^{2+\beta}f) - (2+\beta)r^{1+\beta}f\right], \tag{2.35}$$

where we have substituted for the diffusion coefficient κ using equation (2.8). If N particles are initially localized in radius and momentum, i.e.,

$$f(p, r, t)\Big|_{t=0} = \frac{N}{(4\pi r_0 p_0)^2}\,\delta(p - p_0)\delta(r - r_0)\,, \tag{2.36}$$

then the two terms on the right-hand side of equation (2.35) express respectively the "broadening" and "drifting" of the distribution function f as t increases and particles diffuse into the surrounding plasma.

We can quantify this behavior by calculating the instantaneous rates of change of the mean and mean-square radii at time $t = 0$ for particles initially distributed according to equation (2.36). The average value of r^n is given by

$$\overline{r^n}(t) = N^{-1}\int_0^{\infty}\int_0^{\infty}(4\pi r p)^2 f(p, r, t) r^n\, dr\, dp\,, \tag{2.37}$$

which can be combined with equations (2.35) and (2.36) to obtain the instantaneous rate of change

$$\frac{d}{dt}\overline{r^n}\Big|_{t=0} = n(n + 1 + \beta)r_0^{n-2}\kappa(p_0, r_0)\,, \tag{2.38}$$

and in particular

$$\frac{d}{dt}\bar{r}\Big|_{t=0} = (2+\beta)r_0^{-1}\kappa(p_0, r_0)\,, \qquad \frac{d}{dt}\sigma^2\Big|_{t=0} = 2\kappa(p_0, r_0)\,, \tag{2.39}$$

where the rate of change of the variance $\sigma^2 \equiv \overline{(r - \bar{r})^2}$ expresses the broadening of the particle distribution due to diffusion. Since the average drift velocity of the injected particles is equal to the rate of change of the mean radius, we obtain

$$v_{\rm drift}(p, r) = (2+\beta)\frac{\kappa(p, r)}{r}\,. \tag{2.40}$$

The distinction between $v_{\rm diff}$ (eq. [2.34]) and $v_{\rm drift}$ (eq. [2.40]) reflects the way in which particles are selected for the averaging process. The drift velocity is calculated by averaging over a labeled group of particles with radius r and momentum p at time $t = 0$, while the diffusion velocity is calculated by averaging over all of the particles with momentum p crossing the comoving observer's reference plane.

In spite of the technical differences between $v_{\rm diff}$ and $v_{\rm drift}$, they are usually comparable in magnitude, and we can obtain a rough estimate for the diffusion velocity by setting

$$|v_{\rm diff}(p, r)| \sim |v_{\rm drift}(p, r)| \sim \frac{\kappa(p, r)}{r}\,. \tag{2.41}$$

To establish a working definition for the trapping radius r_t, we eliminate the diffusion coefficient in equation (2.41) using equation (2.8), and equate the result with the bulk flow velocity v given by equation (2.7), obtaining

$$r_t(p)\,|v(r_t)| = \kappa(p, r_t)\,|1 - \alpha - \beta|\,, \tag{2.42}$$

where the numerical factor $|1 - \alpha - \beta|$ has been introduced to agree with the detailed results. In the degenerate case $\alpha + \beta = 1$, the diffusion velocity is proportional to the bulk flow velocity. This case has been treated in detail by Cowsik & Lee (1982) and by Webb & Bogdan (1987), and we shall instead examine the behavior of the system when $\alpha + \beta \neq 1$. The trapping radius concept provides a useful framework for the discussion of the competition between diffusion and advection in § 3.

3. MOMENTUM-INDEPENDENT DIFFUSION

In many cases of astrophysical interest, the spatial diffusion coefficient is a weak function of the particle momentum. For example, the diffusion coefficient describing the resonant scattering of relativistic electrons by Alfvén waves varies as $\kappa \propto p^{1/2}$ for waves with a Kraichnan power spectrum and as $\kappa \propto p^{1/3}$ for waves with a Kolmogorov distribution (e.g., Eilek 1984). If the relativistic particles are photons of moderate energy instead of electrons, then the scattering cross section and the spatial diffusion coefficient are momentum-independent. Hence the study of momentum-independent diffusion may serve to illustrate some of the general principles involved in astrophysical transport phenomena. Various useful analytic relations can be extracted from the Green's function obtained in § 2 when the spatial diffusion coefficient is independent of the particle momentum, since then the particle diffusion velocity $v_{\rm diff}$ and the trapping radius r_t are also momentum-independent. In particular, setting $K(p) = K_0 =$ constant in equation (2.8) for the diffusion coefficient yields

$$\kappa(r) = K_0\left(\frac{r}{r_0}\right)^{\beta}\,, \tag{3.1}$$

and equation (2.42) for the trapping radius now becomes

$$\frac{r_t}{r_0} = \left| \frac{(1-\alpha-\beta)K_0}{r_0 v_0} \right|^{1/(1-\alpha-\beta)} . \tag{3.2}$$

According to equations (2.41) and (3.1), the magnitude of the particle diffusion velocity in this case is given roughly by

$$|v_{\rm diff}| \sim \kappa r^{-1} \propto r^{\beta-1} . \tag{3.3}$$

It is therefore convenient to introduce the new spatial variable

$$\xi(r) \equiv \left(\frac{r}{r_t}\right)^{1-\alpha-\beta} \sim \left| \frac{v}{v_{\rm diff}} \right| , \tag{3.4}$$

where v is the background flow velocity (eq. [2.7]). The magnitude of ξ determines the relative importance of advection and diffusion as particle transport mechanisms. At the trapping radius, $\xi = 1$, and the two processes carry comparable particle fluxes. For $\xi \gtrsim 1$, bulk advection by the background flow dominates diffusion, and the particles are "trapped" within the flow; for $\xi \lesssim 1$, diffusion dominates the particle transport. Whether the trapped, advection-dominated region corresponds to $r > r_t$ or to $r < r_t$ depends on the sign of $1-\alpha-\beta$, or equivalently on the sign of $\eta \equiv (1-\alpha-\beta)/(2-\alpha)$ (eq. [2.27]), since we have assumed that $2-\alpha > 0$ in equation (2.7). In an outflowing plasma with $\eta < 0$, we expect that no particles reach zero radius because outward-bound advection dominates the particle transport as $r \to 0$. Conversely, in an inflowing plasma with $\eta > 0$, we expect that no particles reach *infinite* radius because inward-bound advection dominates as $r \to \infty$. In either case, the net flux of particles in the corresponding region of the flow vanishes once a steady state is achieved, because particles cannot diffuse upstream asymptotically in a region increasingly dominated by advection. Schneider & Bogdan (1989) justifiably used this point to warrant neglect of the "inverted trapping" ($\eta > 0$) case in their study of relativistic particle acceleration in accretion flows, since they were primarily interested in the spectrum of the escaping cosmic rays. However, we shall argue that in the case of electron acceleration, an observable flux of *synchrotron* radiation can be produced even when $\eta > 0$, despite the existence of the "trapping inversion" which prevents the electrons from escaping. For this reason we give results for both positive and negative values of η throughout the remainder of the paper.

In this section we derive results for the momentum integrals of the Green's function, $\mathscr{I}_t(r) \propto \int_0^\infty p^t f_{\rm G}(p, r) dp$, for the case of momentum-independent diffusion, including the effects of quadratic losses. These momentum integrals can be used to obtain the total particle number and energy densities and the total power in radiative losses as functions of radius. They can also be used to obtain results for the steady state distribution function resulting from the continual injection of particles with a power-law spread in momentum. In § 4 we calculate the associated self-consistent synchrotron emissivity for monoenergetic and power-law electron injection.

3.1. *Momentum Integrals of the Green's Function*

With $K(p) = K_0$, the Green's function (eq. [2.29]) describing the transport of relativistic particles injected with Lorentz factor ψ_0 by a source at radius r_0 can be rewritten in terms of ξ (eq. [3.4]) and the new momentum variable

$$s(\psi) \equiv \left[\left(\frac{1}{\psi} - \frac{1}{\psi_c} \right) \Big/ \left(\frac{1}{\psi_0} - \frac{1}{\psi_c} \right) \right]^{-3\eta} , \tag{3.5}$$

as

$$f_{\rm G}(\psi, \xi) = \frac{3\dot{N}_0 |\eta| \, |1 - \psi/\psi_c|^{-1} \xi^{\mu/2}}{(4\pi r_0)^2 |v_0| m_e^3 c^3 \psi^3} \frac{(s\xi_0)^{1-\mu/2}}{|s-1|} \exp\left(- \left| \frac{\xi_0 + s\xi}{s-1} \right| \right) I_\mu \left(\frac{2\sqrt{\xi\xi_0 s}}{|s-1|} \right) , \tag{3.6}$$

where

$$\xi_0 \equiv \left| \frac{r_0 v_0}{(2-\alpha)\eta K_0} \right| . \tag{3.7}$$

Payne & Blandford (1981) derived this solution for the special case of inflow with $\alpha + \beta = 2$ and $\psi_c \to \infty$, which describes the acceleration of photons in spherical accretion flows. Kirk (1987) obtained a version of the Payne and Blandford solution corresponding to particle injection at infinity.

As an application of our Green's function solution, consider the acceleration of electrons in a galaxy cluster cooling flow. Relativistic electrons in cooling flows lose energy by emitting synchrotron photons and by inverse-Compton scattering microwave background photons; in regions where the local magnetic field strength exceeds ~ 3 μG, the magnetic energy density surpasses the energy density of the background radiation, and synchrotron losses dominate (see eq. [2.10]). We can treat this case using our formalism if the variation of the magnetic field is given by

$$B(r) = B_0 \left(\frac{r}{r_0} \right)^{(-1-\alpha)/2} \propto \sqrt{\frac{v}{r}} , \tag{3.8}$$

where B_0 denotes the field strength at the injection radius. Theoretical cooling flow calculations (Soker & Sarazin 1990; White & Sarazin 1987) indicate that the magnetic field and the flow velocity vary with radius approximately as

$$B \propto v \propto r^{-1} , \tag{3.9}$$

which is consistent with equation (3.8) if $\alpha = 1$.

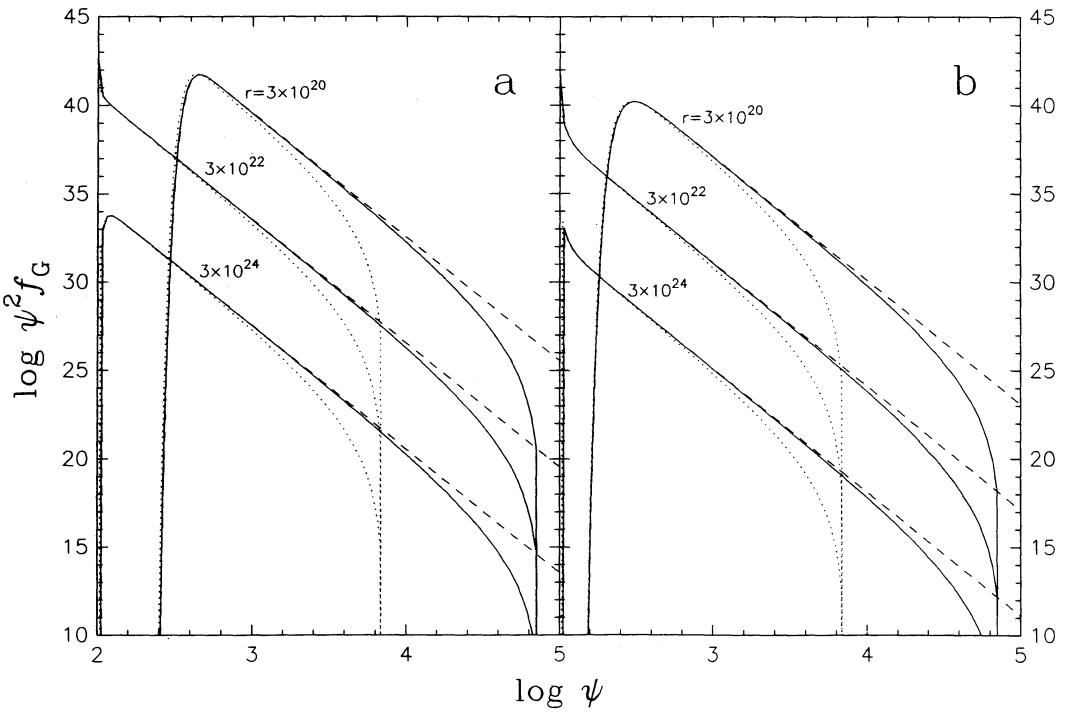

FIG. 2.—Green's function f_G (eq. [3.6]) describing the acceleration and momentum-independent diffusion of electrons injected into a cooling flow with $\psi_0 = 100$, $\alpha = 1$, $r_0 = 3 \times 10^{22}$ cm, $v_0 = -350$ km s^{-1}, $\dot{N}_0 = 10^{47}$ s^{-1}, $\eta = -2$, and (*a*) $K_0 = 1.75 \times 10^{29}$ cm^2 s^{-1}, (*b*) $K_0 = 5.25 \times 10^{30}$ cm^2 s^{-1}, plotted (cgs units) as a function of the electron Lorentz factor ψ. Results are presented for $B_0 = 0$ (*dashed line*), $B_0 = 2.0$ μG (*solid line*), and $B_0 = 6.5$ μG (*dotted line*). The radius (cm) is indicated for each curve.

In Figures 2 and 3, we plot the Green's function (eq. [3.6]) describing the acceleration and momentum-independent diffusion of electrons injected into a cooling flow with Lorentz factor $\psi_0 = 100$ when the momentum losses are due to synchrotron emission and the magnetic field and flow velocity satisfy equation (3.9). For these cooling-flow cases, we have set $\alpha = 1$, $r_0 = 3 \times 10^{22}$ cm, $v_0 = -350$ km s^{-1}, $\dot{N}_0 = 10^{47}$ s^{-1}, and $\eta = -2$ (Fig. 2), $\eta = 2$ (Fig. 3). The injection radius $r_0 \sim 10$ kpc, which is consistent with the magnetic field reconnection radius found by Soker & Sarazin (1990). Magnetic fields of several μG are typical of radio clusters (e.g., Sarazin 1986), and we present results for three values of the injection-radius magnetic field, $B_0 = 0$ (*dashed line*), $B_0 = 2.0$ μG (*solid line*), and $B_0 = 6.5$ μG (*dotted line*). The corresponding values of the critical Lorentz factor (eq. [2.17]) are $\psi_c = \infty$, 7.52×10^4, 7.12×10^3, respectively; note that the electron injection is subcritical since $\psi_0 < \psi_c$. In the absence of losses ($B_0 = 0$, $\psi_c \rightarrow \infty$), a power-law tail develops at large momenta everywhere in the flow as expected, due to in situ acceleration. When finite quadratic losses are included, the power-law tail steepens near $\psi = \psi_c$, where the net acceleration rate (eq. [2.16]) vanishes. The power-law index $\partial \ln f_G / \partial \ln \psi = -9, -6$ in Figures 2 and 3, respectively, in agreement with equation (2.31) for Γ_∞.

The effect of trapping on the particle distribution depends on the relative importance of diffusion and advection at the injection radius, which is parameterized by the value of ξ_0 (eq. [3.7]). Since we have selected fixed values for r_0, v_0, α, and $|\eta|$, the value of ξ_0 depends on the magnitude of the injection-radius diffusion coefficient K_0, which is difficult to estimate in cooling flows. We have chosen the somewhat arbitrary values $K_0 = 1.75 \times 10^{29}$ cm^2 s^{-1} ($\xi_0 = 3$) in Figure 2*a*, $K_0 = 5.25 \times 10^{30}$ cm^2 s^{-1} ($\xi_0 = 0.1$) in Figure 2*b*, $K_0 = 1.75 \times 10^{29}$ cm^2 s^{-1} ($\xi_0 = 3$) in Figure 3*a*, and $K_0 = 1.75 \times 10^{30}$ cm^2 s^{-1} ($\xi_0 = 0.3$) in Figure 3*b*. In both Figures 2 and 3, the overall normalization of the particle spectrum at the injection radius decreases as K_0 increases, since higher levels of diffusion allow more particles to drain away from the point of injection. In the $\eta < 0$ case (Fig. 2), the low-energy cutoff shifts upward as $r \rightarrow 0$, and this shift becomes larger (i.e., more nearly adiabatic) as K_0 decreases (Fig. 2*a*) and trapping becomes more effective. In Figure 3, the degree of attenuation of the Green's function in the outer region of the flow increases dramatically as K_0 decreases (from Fig. 3*b* to Fig. 3*a*), due to the "trapping inversion" operative when $\eta > 0$.

Introducing the momentum integrals of the distribution function,

$$\mathcal{I}_l(\xi) = \int_0^\infty \psi^l f(\psi, \xi) d\psi \,, \tag{3.10}$$

we can express the electron number and energy densities as

$$n(\xi) = 4\pi m_e^3 c^3 \mathcal{I}_2(\xi) \,, \qquad u(\xi) = 4\pi m_e^4 c^5 \mathcal{I}_3(\xi) \,, \tag{3.11}$$

respectively, where we have used the relativistic formula $\epsilon = pc$ for the particle energy. The rate at which the electrons lose energy density via the quadratic loss mechanism (eqs. [2.11] and [2.14]) can be written in terms of $\mathcal{I}_4$ as

$$\dot{u}_{\rm loss}(\xi) = -\int_0^\infty 4\pi p^2 c \langle \dot{p} \rangle_{\rm loss} f dp = \frac{|1 - \alpha - \beta|}{4\pi r_t^3} \xi^{(\alpha+\beta+2)/(\alpha+\beta-1)} \frac{d\dot{E}}{d\xi} \qquad (\propto \text{ergs cm}^{-3}\ \text{s}^{-1}) \,, \tag{3.12a}$$

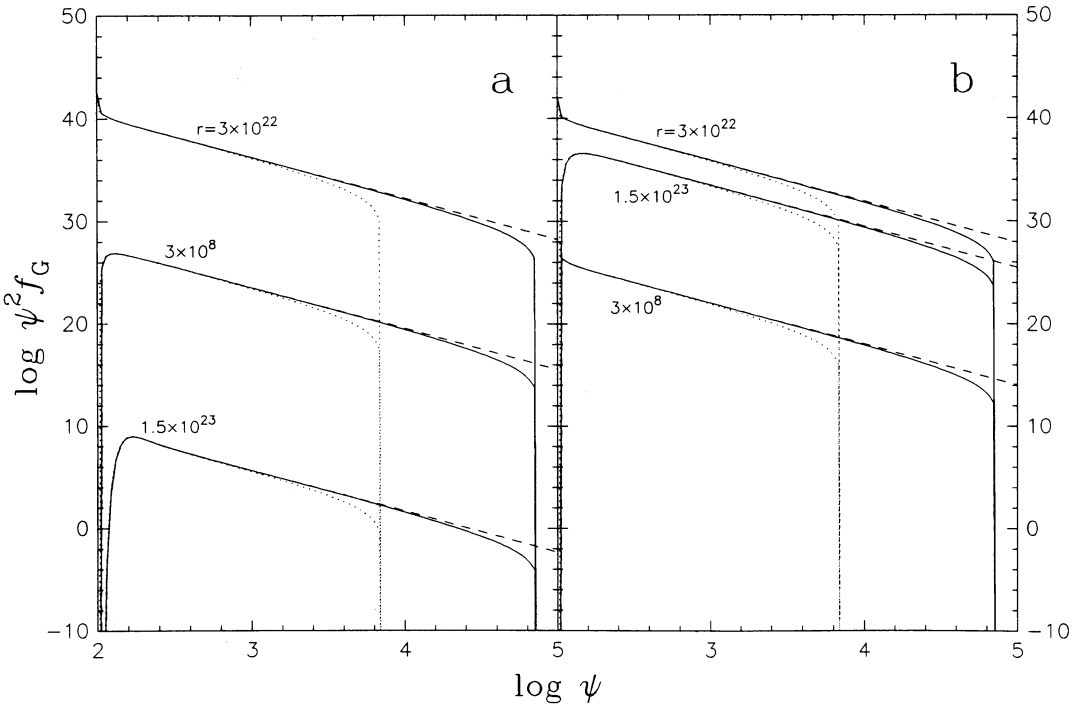

FIG. 3.—Same as Fig. 2, except $\eta = 2$ and (*a*) $K_0 = 1.75 \times 10^{29}$ cm^2 s^{-1}, (*b*) $K_0 = 1.75 \times 10^{30}$ cm^2 s^{-1}

where $\dot{E}$ is the total power expended due to losses by all of the relativistic electrons throughout the flow and

$$\frac{d\dot{E}}{d\xi} = \frac{-(4\pi r_0)^2 m_e^4 c^5 v_0 (\xi/\xi_0)^{-\mu}}{3|\eta|\psi_c \xi_0} \mathscr{I}_4(\xi) \qquad (\propto \text{ergs s}^{-1}) \tag{3.12b}$$

is the differential power. Our relations for u and $\dot{u}_{\rm loss}$ are valid provided the distribution function has no significant nonrelativistic component.

Substituting equation (3.6) for f_G into equation (3.10) and transforming the momentum variable using

$$t(s) \equiv \begin{cases} (s^{-1} - 1)^{-1}, & v_0\eta > 0, \\ (s - 1)^{-1}, & v_0\eta < 0, \end{cases} \tag{3.13}$$

yields

$$\mathscr{I}_l(\xi) = C_0 \xi_0 \left(\frac{\xi}{\xi_0}\right)^{\mu/2} \begin{cases} e^{-\xi_0} \displaystyle\int_0^\infty \left[\frac{1}{\psi_c} + \left(\frac{1}{\psi_0} - \frac{1}{\psi_c}\right)\left(\frac{t}{t+1}\right)^{-1/3\eta}\right]^{2-l} \left(\frac{t}{t+1}\right)^{-\mu/2} T_\mu(\xi, \xi_0, t) \frac{dt}{t+1}, & v_0\eta > 0, \\ e^{-\xi} \displaystyle\int_0^\infty \left[\frac{1}{\psi_c} + \left(\frac{1}{\psi_0} - \frac{1}{\psi_c}\right)\left(\frac{t+1}{t}\right)^{-1/3\eta}\right]^{2-l} \left(\frac{t+1}{t}\right)^{-\mu/2} T_\mu(\xi, \xi_0, t) \frac{dt}{t}, & v_0\eta < 0, \end{cases} \tag{3.14}$$

where we have introduced the function

$$T_\mu(\xi, \xi_0, t) \equiv \exp\left[-(\xi + \xi_0)t\right] I_\mu\left[2\sqrt{\xi\xi_0 t(t+1)}\right], \tag{3.15}$$

and made the definition

$$C_0 \equiv \frac{\dot{N}_0}{(4\pi r_0)^2 m_e^3 c^3 |v_0|}. \tag{3.16}$$

The dependence of $\mathscr{I}_l(\xi)$ on the sign of v_0 enters through equation (2.17) for ψ_c. Recall that $d\ln\xi/d\ln r = 1 - \alpha - \beta = (2 - \alpha)\eta$ according to equation (3.4). Hence ξ is a monotonically increasing function of r if $\eta > 0$, and a monotonically decreasing function of r otherwise, since we have assumed that $2 - \alpha > 0$ in equation (2.7) for the flow velocity. The functional form of $\mathscr{I}_l(r)$ therefore depends sensitively on the signs of both v_0 and η.

3.1.1. *Negligible Losses*

In the absence of losses, $|\psi_c| \to \infty$, and the integrals in equation (3.14) converge provided l and η satisfy

$$\frac{l-2}{3\eta} + 1 > 0, \qquad v_0\eta > 0, \tag{3.17a}$$

$$\frac{l+1}{3\eta} - 1 < 0, \qquad v_0\eta < 0. \tag{3.17b}$$

These constraints arise due to the behavior of the integrands as $t \to 0$, and are trivially satisfied for cases involving an outflowing background plasma, i.e., $v_0 > 0$. However, when the background plasma is inflowing ($v_0 < 0$), meaningful restrictions on η come into play, which are related to the asymptotic behavior of the Green's function as $\psi \to \infty$. In particular, we find that when $v_0 < 0$, the total number density of the relativistic particles diverges for η in the range $0 \leq \eta \leq 1$, and the total energy density diverges for $-1/3 \leq \eta \leq 4/3$. These results are consistent with the behavior of the asymptotic spectral index discussed in § 2.5. (see eq. [2.31] and Fig. 1) for the case of momentum-independent diffusion.

When l and η satisfy equation (3.17), the integrals in equation (3.14) can be evaluated using equation (4.17.15) from Erdélyi et al. (1954), yielding

$$\mathscr{I}_l(\xi) = C_0 \psi_0^{l-2} \xi_0 \xi^{\mu} \begin{cases} e^{-\xi_0} Y_{\mu}(l, \xi, \xi_0) , & v_0 \eta > 0 , \\ e^{-\xi} Y_{\mu}(1-l, \xi, \xi_0) , & v_0 \eta < 0 , \end{cases} \tag{3.18}$$

where $\mu \equiv 1 - 1/\eta$,

$$Y_{\mu}(k, \xi, \xi_0) \equiv \left[\Gamma\left(1 + \frac{k-2}{3\eta}\right) \Big/ \Gamma(\mu + 1) \right] M\left(1 + \frac{k-2}{3\eta}, \mu + 1, \xi_<\right) U\left(1 + \frac{k-2}{3\eta}, \mu + 1, \xi_>\right) , \tag{3.19a}$$

$$\xi_< \equiv \text{Min}\,(\xi, \xi_0) , \qquad \xi_> \equiv \text{Max}\,(\xi, \xi_0) , \tag{3.19b}$$

and M and U are confluent hypergeometric functions (Abramowitz & Stegun 1970). In Figure 4 we use these relations to plot the particle number density n (eq. [3.11], *solid line*), the total particle energy density u (eq. [3.11], *dashed line*), and the average particle energy $\bar{\epsilon} = u/n$ (*dot-dashed line*) as functions of ξ for lossless winds and accretion flows with $\eta = \pm 2$. All of the plots are normalized to unity at the injection radius $r = r_0$, which corresponds to $\xi = \xi_0 = 3$. Note that the average particle energy increases on both sides of the injection radius r_0 in the accretion cases (Figs. 4*a* and 4*b*), regardless of the sign of η. The increase in $\bar{\epsilon}$ is unbounded in the advection-dominated region of the flow ($r \to \infty$ for $\eta > 0$; $r \to 0$ for $\eta < 0$) due to particle trapping. In the diffusion-dominated region of the flow, $\bar{\epsilon}$ attains a maximum value as the relativistic particles decouple from the background plasma. In particular, when $v_0 < 0$ and $\eta > 0$, the number and energy densities each reach a maximum value and then decline to zero as $r \to 0$. The turnover in the density functions in this case is due to the rapid increase in the efficiency of diffusion near the center of the flow. We shall check these conclusions below by calculating the particle flux associated with the Green's function in the case of momentum-independent diffusion.

3.1.2. *Finite Quadratic Losses*

We can evaluate the integrals in equation (3.14) for finite ψ_c by expanding the factors in square brackets as Taylor series. This technique allows us to express the momentum integral $\mathscr{I}_l$ as a power series involving functions of the type introduced in equation

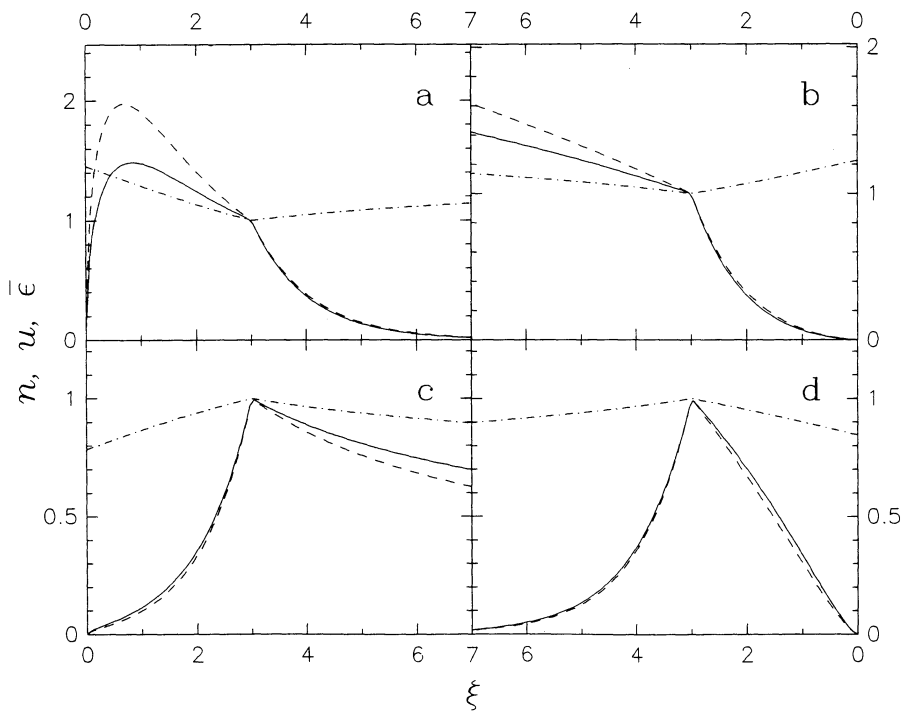

FIG. 4.—Particle number density n (eq. [3.11], *solid line*), energy density u (eq. [3.11], *dashed line*), and average energy $\bar{\epsilon} = u/n$ (*dot-dashed line*) plotted as functions of the spatial coordinate ξ (eq. [3.4]) for cases involving momentum-independent diffusion and negligible losses. The curves are all normalized to unity at the injection radius $\xi = \xi_0 = 3$. The panels describe, in turn, (*a*) inflow ($v_0 < 0$) with $\eta = 2$, (*b*) inflow with $\eta = -2$, (*c*) outflow ($v_0 > 0$) with $\eta = 2$, and (*d*) outflow with $\eta = -2$. The radius r increases to the right in each panel (see eq. [3.4]).

(3.18). The resulting series converges absolutely within a well-defined region of (ψ_0, ψ_c) space. The procedure is straightforward, and after some algebra we obtain

$$\mathscr{I}_l(\xi) = C_0 |\psi_c|^{l-2} \xi_0 \xi^\mu \sum_{m=0}^{\infty} \frac{(l-2)_m}{m!} \begin{cases} e^{-\xi_0}\left(1 - \dfrac{\psi_c}{\psi_0}\right)^{2-l-m} Y_\mu(l+m, \xi, \xi_0)\,, & v_0 > 0,\ \eta > 0\,, \\ e^{-\xi}\left(1 - \dfrac{\psi_c}{\psi_0}\right)^{2-l-m} Y_\mu(1-l-m, \xi, \xi_0)\,, & v_0 > 0,\ \eta < 0\,, \\ e^{-\xi_0}\left(1 - \dfrac{\psi_c}{\psi_0}\right)^{m} Y_\mu(2-m, \xi, \xi_0)\,, & v_0 < 0,\ \eta < 0\,, \\ e^{-\xi}\left(1 - \dfrac{\psi_c}{\psi_0}\right)^{m} Y_\mu(m-1, \xi, \xi_0)\,, & v_0 < 0,\ \eta > 0\,, \end{cases} \tag{3.20}$$

where Y_μ is given by equation (3.19) and $(l-2)_m$ denotes Pochhammer's symbol (Abramowitz & Stegun 1970). The conditions required for absolute convergence of the power series for $\mathscr{I}_l$ are trivially satisfied when the background plasma is outflowing ($v_0 > 0$; upper two expressions eq. [3.20]). However, when the background plasma is *inflowing*, the power series *diverges* if either $\psi_0 \le \psi_c/2$ or $0 \le \eta \le 1$. In the former case, the integrals in equation (3.14) can still be performed numerically, even though the power series representation diverges. However, in the latter case, the total particle number density is infinite, and no steady-state solution exists. When $l = 2$, equation (3.20) for $\mathscr{I}_l$ reduces to equation (3.18), since losses have no effect on the number density $n \propto \mathscr{I}_2$ when the diffusion coefficient is independent of momentum.

The total particle number density n (eq. [3.11], *solid line*), the total particle energy density u (eq. [3.11], *dashed line*), and the average particle energy $\bar{\epsilon} = u/n$ (*dot-dashed line*) are plotted as functions of ξ in Figure 5 for winds and accretion flows with $\eta = \pm 2$ subject to supercritical injection with $\psi_0 = 2|\psi_c|$. Figure 5 also includes plots of the differential power radiated in losses, $d\dot{E}/d\xi$ (eq. [3.12b], *dotted line*). All of the plots are normalized to unity at the injection radius $\xi_0 = 3$. Note that even in the accretion cases (Figs. 5*a* and 5*b*), the average particle energy *decreases* on both sides of the injection radius regardless of the sign of η, because the momentum of the injected particles exceeds the critical momentum. However, the number density profiles in Figure 5 are identical to those in Figure 4, since the diffusion coefficient is independent of momentum. We can shed some light on the nature of the particle transport for the various parameter regimes by computing the total particle flux associated with the Green's function for the case of momentum-independent diffusion.

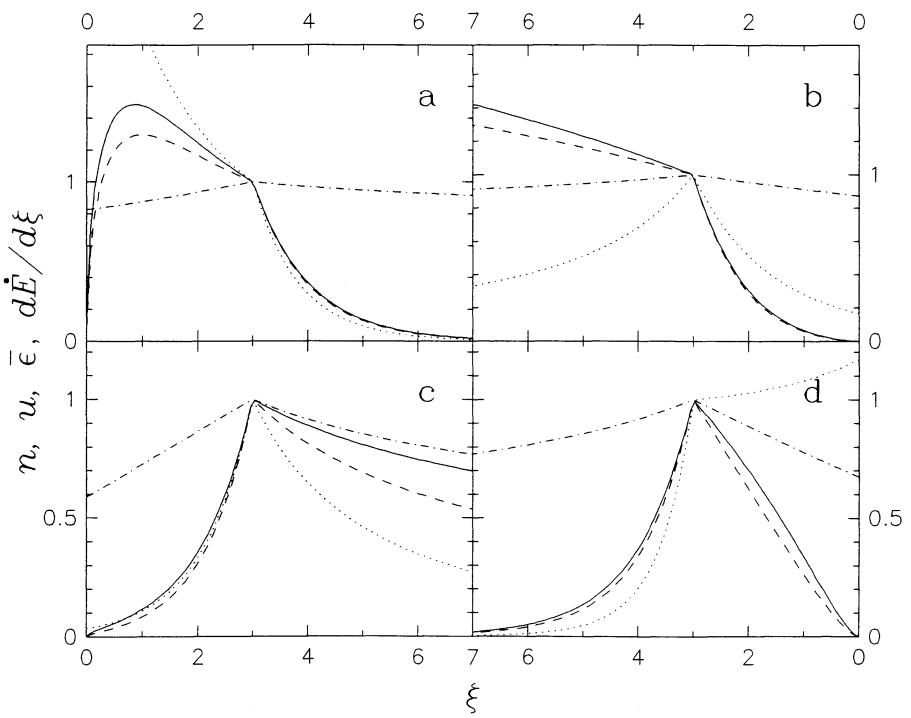

FIG. 5.—Same as Fig. 4, except finite quadratic losses have been included, with $|\psi_c| = 0.5\psi_0$. The panels incorporate plots of the differential power $d\dot{E}/d\xi$ (eq. [3.12b], *dotted line*) normalized to unity at the injection radius.

TABLE 1

SPATIAL VARIATION OF THE NUMBER DENSITY FOR MOMENTUM-INDEPENDENT DIFFUSION

sgn (v_0)	sgn (η)	$n(r < r_0) \propto$	$n(r > r_0) \propto$	$\dot{N}(r < r_0)$	$\dot{N}(r > r_0)$
+1.....	+1	$e^{\xi}\gamma(\mu, \xi)$	$e^{\xi}\Gamma(\mu, \xi)$	$-\Gamma(\mu, \xi_0)\dot{N}_0/\Gamma(\mu)$	$\gamma(\mu, \xi_0)\dot{N}_0/\Gamma(\mu)$
+1.....	−1	$e^{-\xi}$	$e^{-\xi}\gamma(\mu, -\xi)$	0	$\dot{N}_0$
−1.....	−1	$e^{\xi}\Gamma(\mu, \xi)$	$e^{\xi}\gamma(\mu, \xi)$	$-\gamma(\mu, \xi_0)\dot{N}_0/\Gamma(\mu)$	$\Gamma(\mu, \xi_0)\dot{N}_0/\Gamma(\mu)$
−1.....	+1	$e^{-\xi}\gamma(\mu, -\xi)$	$e^{-\xi}$	$-\dot{N}_0$	0

3.2. *Advection versus Diffusion*

The total flux of particles crossing a shell at radius r is given by

$$F_{\rm part} = \int_0^\infty 4\pi p^2 F(p, r) dp = vn - \kappa \frac{dn}{dr} \qquad (\propto s^{-1}\ cm^{-2}), \tag{3.21}$$

where we have substituted for the phase space flux F using equation (2.2). The associated particle transport rate is therefore given by

$$\dot{N} = 4\pi r^2 F_{\rm part} = 4\pi r_0^2 v_0 \left(\frac{\xi}{\xi_0}\right)^{1/\eta} \left[n - \mathrm{sgn}\,(v_0\eta)\frac{dn}{d\xi}\right] \qquad (\propto s^{-1}). \tag{3.22}$$

We can understand the qualitative features of the particle transport for the various combinations of sgn (η) and sgn (v_0) by examining the behavior of the particle number density, $n \propto \mathcal{I}_2$. When $l = 2$, equations (3.18) and (3.20) reduce to the combinations of exponentials and incomplete gamma functions listed in Table 1 (using the notation of Abramowitz and Stegun). Also included in Table 1 are the results for the total (convective plus diffusive) particle transport rate $\dot{N}$ calculated using equation (3.22). In each case, the sum of the magnitudes of the (constant) transport rates at large and small radii equals $\dot{N}_0$, the total particle injection rate at $r = r_0$. When $v_0 > 0$ and $\eta < 0$, the particle flux in the inner region ($r < r_0$) vanishes. Conversely, when $v_0 < 0$ and $\eta > 0$, the particle flux in the outer region ($r > r_0$) vanishes. In each of these cases, the flux vanishes because particles cannot diffuse upstream asymptotically in a region of the flow increasingly dominated by advection, in agreement with the discussion following equation (3.4). Eventually, a steady state is established with a fixed number of particles populating the zero-flux region. This effect also explains the exponential attenuation of $\mathcal{I}_l$ as $\xi \to \infty$ when $v_0\eta < 0$.

In Figure 6 we plot the ratio of the rate at which particles escape from the flow divided by the rate at which particles disappear into the central singularity as a function of ξ_0 and $\mu \equiv 1 - 1/\eta$ for $v_0\eta > 0$. As ξ_0 increases, trapping becomes more effective at the injection radius, and advection therefore carries a larger fraction of the total flux. Since advection transports particles in the direction of the background flow, the magnitude of the escaping fraction depends on the sign of the flow velocity. Figure 6 indicates that the fraction of particles escaping from an accretion flow with $\eta < 0$ (i.e., $\mu > 1$) decreases with increasing ξ_0, since the motion of

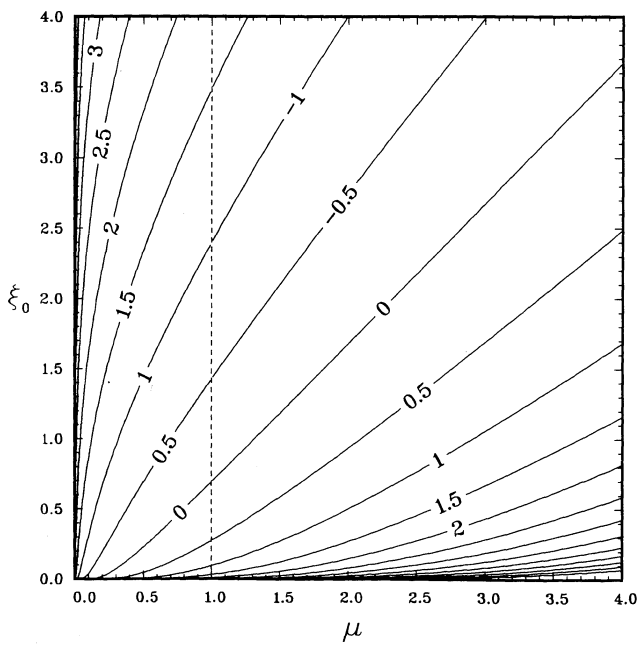

FIG. 6.—Contour plots of the logarithm of the ratio of the escaping fraction of particles divided by the accreting fraction as a function of ξ_0 (eq. [3.7]) and $\mu \equiv 1 - 1/\eta$ for cases with $v_0\eta > 0$. The values of η and v_0 are both positive to the left of the dashed vertical line and negative to the right.

the background plasma tends to sweep particles toward the center of the flow. Conversely, in a wind with $\eta > 0$ ($\mu < 1$), the fraction of particles escaping *increases* with increasing ξ_0, since in this case advection transports particles in an outward direction.

Although cases involving the transport of relativistic electrons injected with a power-law energy distribution generally possess the most direct observational relevance, the Green's function probes the physics in its purest form, since f_G describes the response of the system to monoenergetic particle injection. In order to obtain a detailed understanding of the effects of acceleration and trapping on the particle distribution, it is therefore useful to perform "experiments" that focus on the response of the Green's function to variations in the theoretical parameters. The plots in Figures 2 and 3 demonstrate the effect on the cooling-flow Green's function of varying either the injection-radius field strength B_0 or the injection-radius diffusion coefficient K_0 while holding all of the other parameters (i.e., r_0, v_0, α, η, ψ_0, $\dot{N}_0$) constant. However, in order to compare our results with previous results for particle transport in static background plasmas (e.g., Wilson 1975), a more useful procedure is to vary the injection-radius flow velocity v_0 while holding all of the other parameters fixed. According to equations (2.17) and (3.7), an increase in $|v_0|$ will be accompanied by increases in both ψ_c and ξ_0. The increase in ψ_c will cause the particle energy spectrum to harden, while the increase in ξ_0 will enhance the level of trapping at the injection radius and thereby modify the particle density in the outer regions of the cooling flow. For $\xi_0 \lesssim 1$, most of the injected particles diffuse outward to infinity, and a small increase in ξ_0 causes an increase in the particle density by reducing the number of particles that escape. For $\xi_0 \gtrsim 1$, most of the injected particles are advected into the central singularity, and a small increase in ξ_0 causes a *decrease* in the particle density by increasing the number of particles swept toward the center. It is apparent that the nature of the variations in the Green's function resulting from changes in v_0 will depend on the details of the competition between the various energetic and spatial effects.

In Figure 7 we plot the Green's function (eq. [3.6]) describing the acceleration and momentum-independent diffusion of electrons injected into a cooling flow with $\psi_0 = 100$, $\alpha = 1$, $r_0 = 3 \times 10^{22}$ cm, $B_0 = 6.5$ μG, $\dot{N}_0 = 10^{47}$ s^{-1}, $K_0 = 1.75 \times 10^{29}$ cm^2 s^{-1}, and $\eta = -2$ (Fig. 7*a*), $\eta = 2$ (Fig. 7*b*). Results are presented for two values of the injection-radius flow velocity, $v_0 = -35$ km s^{-1} (*dotted line*) and $v_0 = -350$ km s^{-1} (*solid line*), with $\psi_c = 7.12 \times 10^2$, $\xi_0 = 0.3$, and $\psi_c = 7.12 \times 10^3$, $\xi_0 = 3$, respectively. The energetic effect of increasing $|v_0|$ is straightforward; the particle spectrum extends to higher energies when $v_0 = -350$ km s^{-1}, regardless of the sign of η. However, the response of the spatial distribution of the electrons to changes in v_0 is markedly different depending on the sign of η. When $\eta < 0$ (Fig. 7*a*), the larger value of ξ_0 produces only a slight reduction in the density of particles at large radii; when $\eta > 0$ (Fig. 7*b*), the decrease is quite dramatic.

In order to further clarify the effects of trapping and acceleration on the cooling-flow Green's function, in Table 2A we give results for the total synchrotron luminosity radiated in the outer region of the flow, $\dot{E}(r > r_0)$, (obtained by integrating eq. [3.12b] for the differential power) for sequences of models with decreasing K_0, using the canonical values $\psi_0 = 100$, $\dot{N}_0 = 10^{47}$ s^{-1}, $\alpha = 1$, $r_0 = 3 \times 10^{22}$ cm, $B_0 = 6.5$ μG, and $v_0 = -0.1$ km s^{-1}. The power radiated in the inner region of the flow has been neglected since we are primarily interested in the luminosity of the extended radio structure. Table 2A also includes values for the critical Lorentz factor ψ_c, the fraction of electrons escaping to infinity $\dot{N}(r > r_0)/\dot{N}_0$ (see Table 1), the injection-radius electron number density $n(r_0)$,

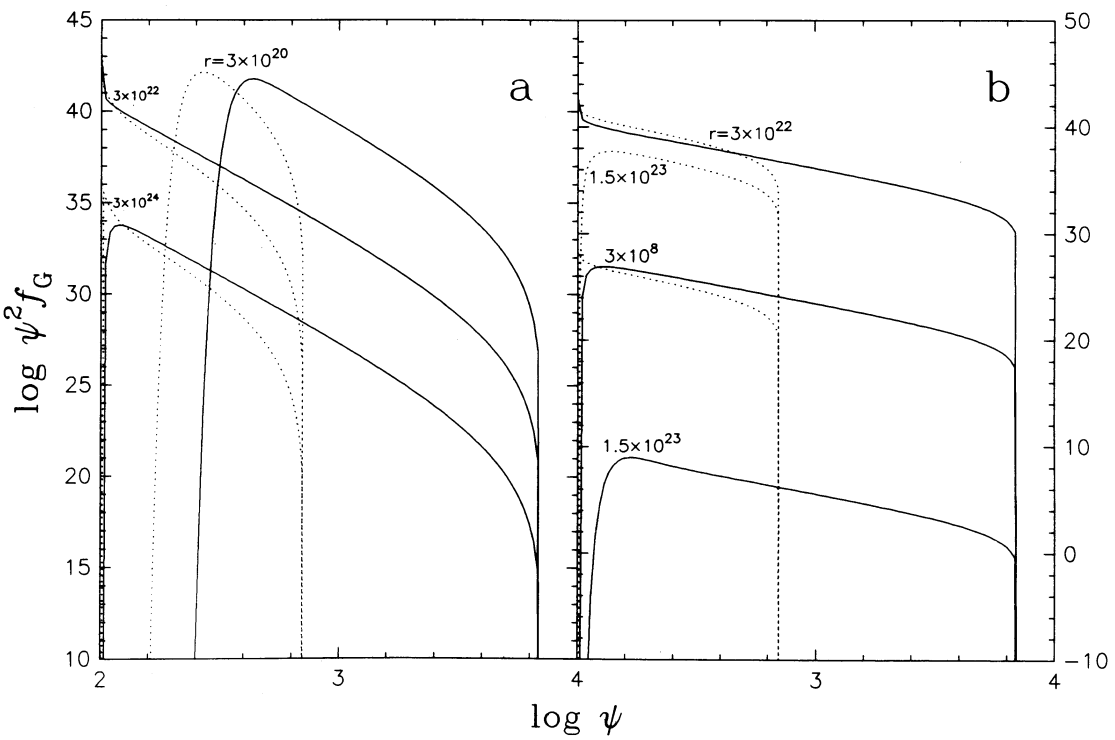

FIG. 7.—Green's function f_G (eq. [3.6]) describing the acceleration and momentum-independent diffusion of electrons injected into a cooling flow with $\psi_0 = 100$, $\alpha = 1$, $r_0 = 3 \times 10^{22}$ cm, $B_0 = 6.5$ μG, $\dot{N}_0 = 10^{47}$ s^{-1}, $K_0 = 1.75 \times 10^{29}$ cm^2 s^{-1}, and (*a*) $\eta = -2$, (*b*) $\eta = 2$, plotted (cgs units) as a function of the electron Lorentz factor ψ. Results are presented for $v_0 = -35$ km s^{-1} (*dotted line*) and $v_0 = -350$ km s^{-1} (*solid line*). The radius (cm) is indicated for each curve.

TABLE 2A

MODEL RESULTS FOR MONOENERGETIC INJECTION WITH MOMENTUM-INDEPENDENT DIFFUSION: EFFECT OF VARYING K_0

η	$\dot{N}_0$ (s^{-1})	v_0 (km s^{-1})	ξ_0	K_0 (cm^2 s^{-1})	ψ_c	$\dot{E}(r > r_0)$ (ergs s^{-1})	$\dot{N}(r > r_0)/\dot{N}_0$	$n(r_0)$ (cm^{-3})	$\bar{\psi}(r_0)$	Efficiency
−2.....	10^{47}	−0.1	0.001	1.50×10^{29}	2.0	4.34×10^{40}	100.0%	5.9×10^{-7}	98.5	0.5%
			0.01	1.50×10^{28}	2.0	3.76×10^{41}	99.9	5.9×10^{-6}	92.2	4.6
			0.1	1.50×10^{27}	2.0	1.97×10^{42}	97.8	6.0×10^{-5}	69.0	24.0
			0.8	1.88×10^{26}	2.0	3.51×10^{42}	65.9	4.4×10^{-4}	41.7	42.9
			0.9	1.67×10^{26}	2.0	3.55×10^{42}	61.5	4.8×10^{-4}	40.6	43.4
			1.0	1.50×10^{26}	2.0	3.52×10^{42}	57.2	5.2×10^{-4}	40.0	43.0
+2.....	10^{47}	−0.1	0.001	1.50×10^{29}	2.0	1.07×10^{42}	0.0	1.8×10^{-6}	86.1	13.1
			0.01	1.50×10^{28}	2.0	2.37×10^{42}	0.0	1.8×10^{-5}	66.4	28.9
			0.1	1.50×10^{27}	2.0	3.45×10^{42}	0.0	1.7×10^{-4}	39.5	42.1
			0.2	7.50×10^{26}	2.0	3.52×10^{42}	0.0	3.1×10^{-4}	33.0	43.0
			0.3	5.00×10^{26}	2.0	3.50×10^{42}	0.0	4.4×10^{-4}	30.0	42.7
			0.4	3.75×10^{26}	2.0	3.45×10^{42}	0.0	5.5×10^{-4}	28.3	42.2

the average Lorentz factor at the injection radius $\bar{\psi}(r_0)$, the efficiency of radiative losses $\dot{E}(r > r_0)/(\psi_0 m_e c^2 \dot{N}_0)$, and the parameters η and ξ_0. For all of the cases in Table 2A, $\psi_c = 2.0 \ll \psi_0$, which means that all of the electrons lose energy while they remain in the flow. Furthermore, since K_0 is the only variable fundamental parameter, the net acceleration rate (eq. [2.16]) is the same for all of the models, and therefore any differences in the model results can be directly attributed to changes in the mode of spatial transport (i.e., changes in the level of trapping).

Note that for both positive and negative values of η, the synchrotron luminosities in Table 2A increase with increasing ξ_0 (i.e., decreasing K_0), reaching a maximum at $\xi_0 = 0.9$ ($\eta = -2$), $\xi_0 = 0.2$ ($\eta = 2$), and diminishing for larger values of ξ_0. The rise and subsequent decline of the luminosity is due to two competing effects each associated with the level of trapping, which increases with increasing ξ_0. The first is an increase in the electron density in the outer regions of the flow (since $\xi_0 \lesssim 1$), and the second is a concomitant softening of the electron energy distribution (due to the increased residence time) which reduces $\bar{\psi}(r_0)$. The first effect tends to *increase* the luminosity because more electrons are radiating per unit volume, while the second effect tends to *decrease* the luminosity because the synchrotron power per electron scales as the square of the electron energy (eq. [2.9]). The maximum luminosity (with efficiency $\sim 43\%$) is obtained under conditions corresponding to marginal trapping at the injection radius.

The variations in the synchrotron luminosity in Table 2A are due to changes in the injection-radius diffusion coefficient K_0, which leave the energetics of the acceleration process unchanged. In Table 2B we examine the variations in the synchrotron luminosity produced by changing the injection-radius flow velocity v_0 (which plays a role in both the spatial and energetic transport processes) while holding all of the other parameters constant. We give results for sequences of models with increasing $|v_0|$, beginning with parameters corresponding to the peak luminosities for positive and negative η in Table 2A. Since larger values of $|v_0|$ yield higher net acceleration rates according to equation (2.16), we might expect the synchrotron luminosity to increase with increasing $|v_0|$. However, the synchrotron luminosity actually *decreases* with increasing $|v_0|$ in Table 2B, despite the fact that ψ_c increases and the electron energy distribution hardens significantly. The decrease in luminosity (and efficiency) is due to the enhanced trapping associated with the large values of ξ_0, which greatly reduces the electron density in the outer regions of the cooling flow.

In order to remove the spatial effect of enhanced trapping and thereby focus on the *energetic* effect of increasing the value of $|v_0|$, we need to inhibit the sharp reduction in the electron density apparent in Table 2B. According to equation (3.2), the trapping radius r_t is invariant if $K_0 \propto v_0$. It follows from equations (3.4) and (3.18) that the electron number density $n \propto \mathscr{I}_2$ is invariant if $\dot{N}_0 \propto K_0 \propto v_0$. Motivated by this observation, in Table 2C we present results for the synchrotron luminosity obtained by allowing $\dot{N}_0$ and K_0 to vary in proportion to v_0, beginning with parameters corresponding to the peak luminosities for positive and negative η in Table 2A, and using the values of v_0 listed in Table 2B. As expected, the synchrotron luminosity now increases as $|v_0| \to \infty$ since the number density distribution of the electrons is maintained. The growth in the synchrotron luminosity clearly illustrates the effect of first-order Fermi acceleration due to bulk motions of the background plasma.

TABLE 2B

MODEL RESULTS FOR MONOENERGETIC INJECTION WITH MOMENTUM-INDEPENDENT DIFFUSION: EFFECT OF VARYING v_0

η	$\dot{N}_0$ (s^{-1})	v_0 (km s^{-1})	ξ_0	K_0 (cm^2 s^{-1})	ψ_c	$\dot{E}(r > r_0)$ (ergs s^{-1})	$\dot{N}(r > r_0)/\dot{N}_0$	$n(r_0)$ (cm^{-3})	$\bar{\psi}(r_0)$	Efficiency
−2.....	10^{47}	−0.1	0.9	1.67×10^{26}	2.0	3.55×10^{42}	61.5%	4.8×10^{-4}	40.6	43.4%
		−4.0	36.0	1.67×10^{26}	81.4	4.90×10^{40}	$\sim 10^{-13}$	2.2×10^{-5}	99.8	0.6
		−5.0	45.0	1.67×10^{26}	101.8	3.12×10^{40}	$\sim 10^{-17}$	1.8×10^{-5}	100.0	0.4
		−6.0	54.0	1.67×10^{26}	122.1	2.16×10^{40}	$\sim 10^{-21}$	1.5×10^{-5}	100.1	0.3
+2.....	10^{47}	−0.1	0.2	7.50×10^{26}	2.0	3.52×10^{42}	0.0	3.1×10^{-4}	33.0	43.0
		−4.0	8.0	7.50×10^{26}	81.4	2.09×10^{41}	0.0	2.4×10^{-5}	98.9	2.5
		−5.0	10.0	7.50×10^{26}	101.8	1.36×10^{41}	0.0	1.9×10^{-5}	100.1	1.7
		−6.0	12.0	7.50×10^{26}	122.1	9.59×10^{40}	0.0	1.5×10^{-5}	100.5	1.2

TABLE 2C

MODEL RESULTS FOR MONOENERGETIC INJECTION WITH MOMENTUM-INDEPENDENT DIFFUSION: EFFECT OF VARYING $\dot{N}_0 \propto K_0 \propto v_0$

η	$\dot{N}_0$ (s^{-1})	v_0 (km s^{-1})	ξ_0	K_0 (cm^2 s^{-1})	ψ_c	$\dot{E}(r > r_0)$ (ergs s^{-1})	$\dot{N}(r > r_0)/\dot{N}_0$	$n(r_0)$ (cm^{-3})	$\bar{\psi}(r_0)$	Efficiency
−2.....	1×10^{47}	−0.1	0.9	1.67×10^{26}	2.0	3.55×10^{42}	61.5%	4.8×10^{-4}	40.6	43.4%
	4×10^{48}	−4.0	0.9	6.67×10^{27}	81.4	2.87×10^{43}	61.5	4.8×10^{-4}	98.1	8.7
	5×10^{48}	−5.0	0.9	8.33×10^{27}	101.8	3.02×10^{43}	61.5	4.8×10^{-4}	100.1	7.4
	6×10^{48}	−6.0	0.9	1.00×10^{28}	122.1	3.14×10^{43}	61.5	4.8×10^{-4}	101.6	6.4
+2.....	1×10^{47}	−0.1	0.2	7.50×10^{26}	2.0	3.52×10^{42}	0.0	3.1×10^{-4}	33.0	43.0
	4×10^{48}	−4.0	0.2	3.00×10^{28}	81.4	5.42×10^{43}	0.0	3.1×10^{-4}	96.9	16.6
	5×10^{48}	−5.0	0.2	3.75×10^{28}	101.8	6.05×10^{43}	0.0	3.1×10^{-4}	100.3	14.8
	6×10^{48}	−6.0	0.2	4.50×10^{28}	122.1	6.58×10^{43}	0.0	3.1×10^{-4}	102.9	13.4

3.3. *Localized Power-Law Injection*

The momentum integrals of the Green's function discussed above provide some important insights into the nature of the transport and acceleration processes occurring in accretion flows and winds subject to the injection of monoenergetic test particles. However, in most cases of astrophysical interest, the injected particles are produced and/or preaccelerated by some nonthermal mechanism such as magnetic reconnection or turbulent amplification, and are therefore distributed as a power law in energy rather than as a delta function. A power-law source of electrons at radius r_0 can be written as

$$\dot{f}(p, r) = D_0 \left(\frac{p}{m_e c}\right)^{-L} \delta\left(\frac{r}{r_0} - 1\right), \tag{3.23}$$

where L is the power-law index and D_0 determines the normalization. We shall assume that the background plasma is inflowing ($v_0 < 0$), and restrict our attention to cases involving the injection of electrons with Lorentz factor ψ_0 in the range $0 < \psi_0 < \psi_c$. Furthermore, we shall assume that L is an integer ≥ 4; hence the injected power-law profile contains an infinite number of low-energy particles. These restrictions allow us to obtain closed-form solutions for the resulting steady state particle distribution. Results of a more general nature can, however, be obtained using numerical techniques. The steady state distribution function resulting from the continual injection of electrons from a source described by equation (3.23) is

$$f_S = \frac{(4\pi)^2 D_0 r_0^3 m_e^3 c^3}{\dot{N}_0} \int_0^{\psi_c} f_G \psi_0^{2-L} d\psi_0 . \tag{3.24}$$

Substituting equation (3.6) for f_G into equation (3.24) and transforming the momentum variable to t (eq. [3.13]) yields

$$f_S(\psi, \xi) = \frac{D_0 r_0 \xi_0 (\xi/\xi_0)^{\mu/2}}{|v_0| \psi^4} \begin{cases} e^{-\xi_0} \displaystyle\int_0^\infty \left[\frac{1}{\psi_c} + \left(\frac{1}{\psi} - \frac{1}{\psi_c}\right)\left(\frac{t}{t+1}\right)^{1/3\eta}\right]^{L-4} \left(\frac{t}{t+1}\right)^{(2-5\mu)/6} T_\mu(\xi, \xi_0, t) \frac{dt}{t+1}, & \eta < 0, \\ e^{-\xi} \displaystyle\int_0^\infty \left[\frac{1}{\psi_c} + \left(\frac{1}{\psi} - \frac{1}{\psi_c}\right)\left(\frac{t+1}{t}\right)^{1/3\eta}\right]^{L-4} \left(\frac{t+1}{t}\right)^{(2-5\mu)/6} T_\mu(\xi, \xi_0, t) \frac{dt}{t}, & \eta > 0, \end{cases} \tag{3.25}$$

for the case of an inflowing background plasma, where T_μ is given by equation (3.15). These integrals are related to those appearing in equation (3.14) for $\mathcal{I}_l$. We shall consider the cases of finite and negligible losses separately.

3.3.1. *Negligible Losses*

In the case of inflow with negligible losses ($\psi_c \to \infty$), the integrals in equation (3.25) for f_S converge provided L and η satisfy

$$\frac{L-3}{3\eta} + 1 > 0, \qquad \eta < 0, \tag{3.26a}$$

$$\frac{L}{3\eta} - 1 < 0, \qquad \eta > 0, \tag{3.26b}$$

in which case we obtain

$$f_S(\psi, \xi) = \frac{D_0 r_0 \xi_0 \xi^\mu}{|v_0| \psi^L} \begin{cases} e^{-\xi_0} Y_\mu(L-1, \xi, \xi_0), & \eta < 0, \\ e^{-\xi} Y_\mu(2-L, \xi, \xi_0), & \eta > 0, \end{cases} \tag{3.27}$$

where Y_μ is given by equation (3.19). These results are also valid for noninteger L. Note that the index of the injected power-law distribution is preserved throughout the flow when the diffusion coefficient is independent of momentum and losses are negligible, because under these circumstances the time scales for spatial transport and acceleration are both momentum-independent. Hence electrons are accelerated from low energies at exactly the rate required to compensate for the removal of high-energy electrons from the flow.

3.3.2. *Finite Quadratic Losses*

When ψ_c is finite and the background plasma is inflowing ($v_0 < 0$), we can evaluate the integrals in equation (3.25) by expanding the factors in square brackets. The results obtained are

$$f_S(\psi, \xi) = \frac{D_0 r_0 \xi_0 \xi^\mu \psi_c^{4-L}}{|v_0| \psi^4} \sum_{m=0}^{L-4} \frac{(L-3-m)_m}{m!} \left(\frac{\psi_c}{\psi} - 1\right)^{L-4-m} \begin{cases} e^{-\xi_0} Y_\mu(L-m-1, \xi, \xi_0), & \eta < 0, \\ e^{-\xi} Y_\mu(2+m-L, \xi, \xi_0), & \eta > 0, \end{cases} \tag{3.28}$$

for integer $L \geq 4$. These series converge provided L and η satisfy equation (3.26). If the injected electrons are distributed according to $\dot{f} \propto \psi^{-4}$, then the series for f_S truncates after just one term and $f_S \propto \psi^{-4}$ throughout the entire flow. This behavior stems from the fact that $f \propto p^{-4} \propto \psi^{-4}$ is the equilibrium power-law particle spectrum for the case of pure synchrotron emission with

$$\left(\frac{\partial f}{\partial t}\right)_{\text{synch}} = -\frac{1}{p^2} \frac{\partial}{\partial p} (-AB^2 p^4 f). \tag{3.29}$$

As another example, consider the injection of electrons with $\dot{f} \propto \psi^{-6}$. In this case, the series for f_S truncates after three terms, and the shape of the steady state distribution function *evolves in radius.*

In Figures 8 and 9 we plot the steady state distribution function f_S (eq. [3.28]) describing the acceleration and momentum-independent diffusion of electrons injected into a cooling flow with a power-law spread in momentum. For these cooling-flow cases, we have assumed that the losses are due to synchrotron emission with $B \propto v \propto r^{-1}$, $\alpha = 1$, $r_0 = 3 \times 10^{22}$ cm, $v_0 = -350$ km s^{-1}, $D_0 = 10^{32}$ ergs^{-3} s^{-4}, $K_0 = 1.4 \times 10^{29}$ cm^2 s^{-1} ($\xi_0 = 3$), and $\eta = -2.5$ (Fig. 8), $\eta = 2.5$ (Fig. 9). The power-law index $L = 5$ in Figures 8*a* and 9*a*, while $L = 6$ in Figures 8*b* and 9*b*. Results are presented for three values of the injection-radius magnetic field, $B_0 = 0$ (*dashed line*), $B_0 = 2.0$ μG (*solid line*), and $B_0 = 6.5$ μG (*dotted line*); the corresponding values of the critical Lorentz factor (eq. [2.17]) are $\psi_c = \infty$, 7.52×10^4, 7.12×10^3, respectively. In all cases, we assume that the power-law injection spectrum $\dot{f}$ truncates at $\psi = \psi_c$. As $\psi \to 0, f_S \propto \psi^{-L}$ due to the infinite number of low-energy electrons in the injected profile. When $B_0 \neq 0$, the particle spectrum steepens as $\psi \to \psi_c$ because advection sweeps the highest energy electrons into the central singularity before they can be replaced by lower energy electrons accelerated to $\psi \sim \psi_c$ (Webb & Bogdan 1987). This behavior is in contrast to the usual unity increase in the power-law index associated with losses in a static plasma (e.g., Kardashev 1962). It is interesting to note that the steepening in Figures 8 and 9 is not as severe as that displayed by the Green's functions in Figures 2 and 3, due to the fact that the power-law injection occurs over a broad range of energies up to the cutoff at $\psi = \psi_c$. In the absence of losses ($B_0 = 0, \psi_c \to \infty$), the injected power-law index is preserved throughout the flow, and the particle spectrum extends to infinite energy. Note the strong attenuation at large radii when $\eta > 0$, in agreement with the results for monoenergetic injection discussed above.

In Table 3A we give results for the total synchrotron luminosity radiated by electrons with $\psi \geq 10^3$ in the outer region of the flow for sequences of power-law injection models with decreasing K_0, using the canonical values $L = 5$, $D_0 = 10^{32}$ ergs^{-3} s^{-4}, $\alpha = 1$,

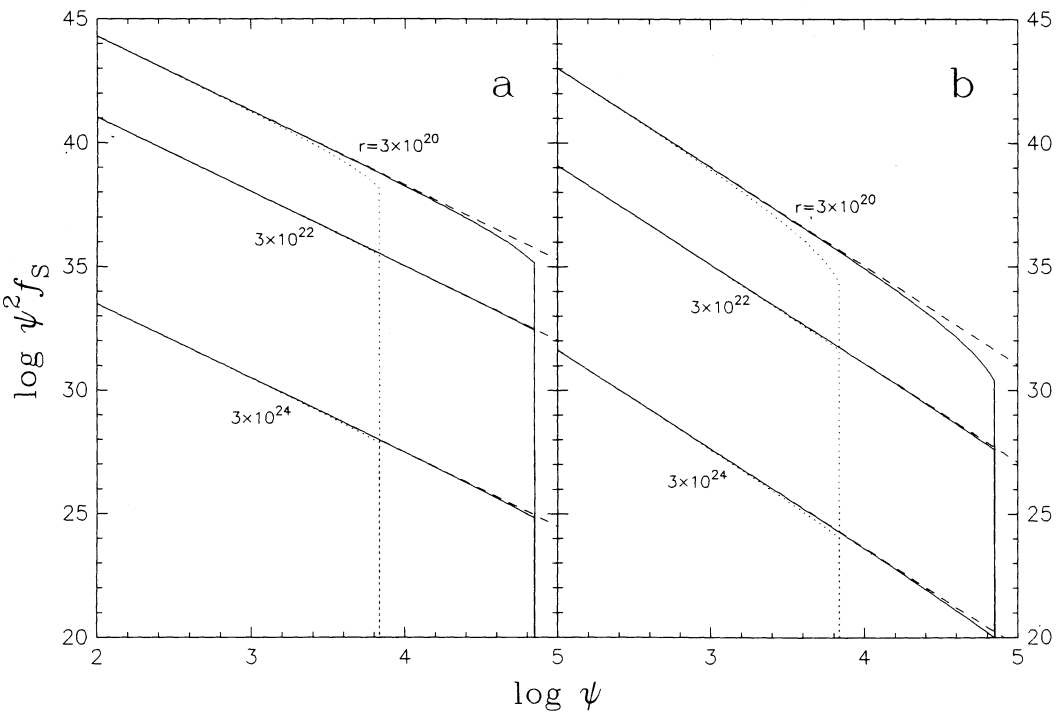

FIG. 8.—Steady state particle distribution f_S (eq. [3.28]) describing the acceleration and momentum-independent diffusion of electrons injected with a power-law spread in momentum into a cooling flow with $\alpha = 1$, $r_0 = 3 \times 10^{22}$ cm, $v_0 = -350$ km s^{-1}, $D_0 = 10^{32}$ ergs^{-3} s^{-4}, $K_0 = 1.4 \times 10^{29}$ cm^2 s^{-1}, $\eta = -2.5$, and (*a*) $L = 5$, (*b*) $L = 6$, plotted (cgs units) as a function of the electron Lorentz factor ψ. Results are presented for $B_0 = 0$ (*dashed line*), $B_0 = 2.0$ μG (*solid line*), and $B_0 = 6.5$ μG (*dotted line*). The radius (cm) is indicated for each curve.

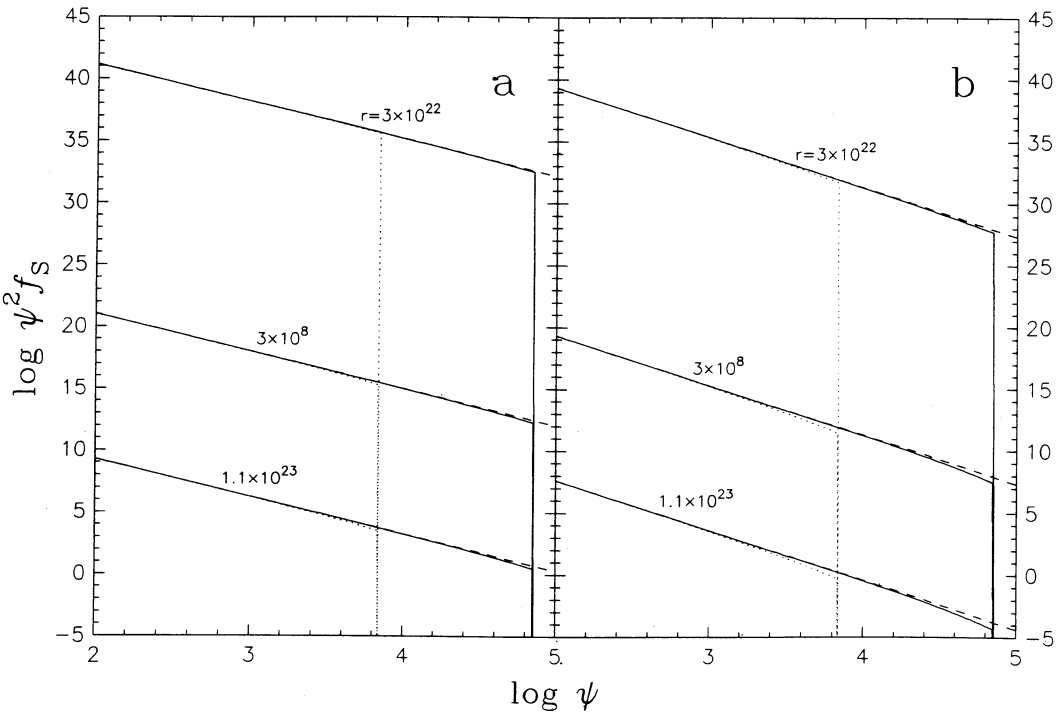

FIG. 9.—Same as Fig. 8, except $\eta = 2.5$

$r_0 = 3 \times 10^{22}$ cm, $B_0 = 6.5$ μG, and $v_0 = -50$ km s^{-1}. The lower bound on ψ ensures that the emission occurs at observable radio frequencies ($\gtrsim 20$ MHz at $r = r_0$). Table 3A also includes values for the critical Lorentz factor ψ_c, the fraction of electrons escaping to infinity $\dot{N}(r > r_0)/\dot{N}_0$, and the parameters η and ξ_0. Since K_0 is the only variable fundamental parameter, the net acceleration rate (eq. [2.16]) is the same for all of the models, and therefore any variations in the results can be directly attributed to changes in the level of trapping. The total synchrotron luminosity increases with increasing ξ_0 (i.e., decreasing K_0), reaching a maximum at $\xi_0 = 2.0$ ($\eta = -2.5$), $\xi_0 = 0.5$ ($\eta = 2.5$), and diminishing for larger values of ξ_0. The rise and subsequent decline of the luminosity as ξ_0 increases is due to the competition between the increasing electron density and the softening electron spectrum. The maximum luminosity is obtained under conditions corresponding to marginal trapping at the injection radius, in agreement with the results for monoenergetic injection.

In Table 3B we calculate the synchrotron luminosity for sequences of power-law injection models with increasing $|v_0|$, beginning with parameters corresponding to the peak luminosities for positive and negative η in Table 3A. The synchrotron luminosity rises and then drops as $|v_0|$ is steadily increased. The initial increase in luminosity is due to the increase in ψ_c, which hardens the electron spectrum. The subsequent drop in luminosity is due to the onset of enhanced trapping, which occurs at $\xi_0 \gtrsim 1$. In § 4 we calculate the self-consistent synchrotron emissivity for monoenergetic and power-law electron injection, and compare the spatial variation of the radio spectrum with the surface brightness distribution reported for the core-halo in the Perseus cluster.

TABLE 3A

MODEL RESULTS FOR POWER-LAW INJECTION WITH MOMENTUM-INDEPENDENT DIFFUSION: EFFECT OF VARYING K_0

η	v_0 (km s^{-1})	ξ_0	K_0 (cm^2 s^{-1})	ψ_c	$\dot{E}(r > r_0)$ (ergs s^{-1})	$\dot{N}(r > r_0)/\dot{N}_0$
−2.5.....	−50.0	0.001	6.00×10^{31}	1017.5	1.16×10^{37}	100.0%
		0.01	6.00×10^{30}	1017.5	1.16×10^{38}	99.9
		0.1	6.00×10^{29}	1017.5	1.17×10^{39}	97.0
		1.0	6.00×10^{28}	1017.5	8.74×10^{39}	53.4
		2.0	3.00×10^{28}	1017.5	1.04×10^{40}	23.4
		3.0	2.00×10^{28}	1017.5	9.10×10^{39}	9.7
+2.5.....	−50.0	0.001	6.00×10^{31}	1017.5	1.04×10^{39}	0.0
		0.01	6.00×10^{30}	1017.5	3.72×10^{39}	0.0
		0.1	6.00×10^{29}	1017.5	1.09×10^{40}	0.0
		0.3	2.00×10^{29}	1017.5	1.49×10^{40}	0.0
		0.5	1.20×10^{29}	1017.5	1.56×10^{40}	0.0
		0.7	8.57×10^{28}	1017.5	1.53×10^{40}	0.0

TABLE 3B

MODEL RESULTS FOR POWER-LAW INJECTION WITH MOMENTUM-INDEPENDENT DIFFUSION: EFFECT OF VARYING v_0

η	v_0 (km s^{-1})	ξ_0	K_0 (cm^2 s^{-1})	ψ_c	$\dot{E}(r > r_0)$ (ergs s^{-1})	$\dot{N}(r > r_0)/\dot{N}_0$
−2.5.....	−50.0	2.0	3.00×10^{28}	1.0×10^3	1.04×10^{40}	23.4%
	−100.0	4.0	3.00×10^{28}	2.0×10^3	1.55×10^{41}	3.9
	−500.0	20.0	3.00×10^{28}	1.0×10^4	1.23×10^{40}	$\sim 10^{-6}$
	−1000.0	40.0	3.00×10^{28}	2.0×10^4	3.74×10^{39}	$\sim 10^{-15}$
+2.5.....	−50.0	0.5	1.20×10^{29}	1.0×10^3	1.56×10^{40}	0.0
	−100.0	1.0	1.20×10^{29}	2.0×10^3	3.20×10^{41}	0.0
	−500.0	5.0	1.20×10^{29}	1.0×10^4	5.28×10^{40}	0.0
	−1000.0	10.0	1.20×10^{29}	2.0×10^4	1.50×10^{40}	0.0

4. SYNCHROTRON EMISSION IN COOLING FLOWS

The particle transport formalism developed in §§ 2 and 3 can be used to study the effects of spatial diffusion, first-order Fermi acceleration, and momentum losses in spherically symmetric winds and accretion flows with momentum loss rates satisfying the quadratic prescription

$$\langle \dot{p} \rangle_{\rm loss}(p, r) = -R_0 \left(\frac{r}{r_0} \right)^{-1-\alpha} p^2 \propto \frac{vp^2}{r} , \tag{4.1}$$

obtained by combining equations (2.11) and (2.14). In § 3 we used our formalism to calculate the steady state particle distributions resulting from monoenergetic and power-law electron injection in galaxy-cluster cooling flows. In this section, we consider the observational implications of our model for the production of synchrotron emission in cooling flows.

4.1. *Synchrotron Emission*

The synchrotron power per unit frequency radiated by a relativistic electron with Lorentz factor ψ and pitch angle θ spiraling in a magnetic field of strength B is (e.g., Rybicki & Lightman 1979)

$$P_\nu(\theta) = \frac{\sqrt{3}\, e^3 B \sin\theta}{m_e c^2} F\left(\frac{\nu}{\psi^2 \nu_s \sin\theta} \right) \qquad (\propto \text{ergs s}^{-1}\ \text{Hz}^{-1}) , \tag{4.2}$$

where

$$F(x) \equiv x \int_x^\infty K_{5/3}(t) dt , \tag{4.3}$$

and

$$\nu_s \equiv \frac{3eB}{4\pi m_e c} = 4.2 \left(\frac{B}{1\ \mu\text{G}} \right) \text{Hz} . \tag{4.4}$$

If the electron distribution function f is isotropic, then the fraction of electrons with pitch angle in the range $d\theta$ is $(d\theta/2) \sin\theta$, and the angle-averaged synchrotron power per unit frequency per electron is therefore

$$\bar{P}_\nu = \frac{\sqrt{3}\, e^3 B}{m_e c^2} W\left(\frac{\nu}{\psi^2 \nu_s} \right) , \tag{4.5}$$

where the angular integration is expressed by the function

$$W(x) \equiv \int_0^1 \frac{\mu^2}{\sqrt{1-\mu^2}} F\left(\frac{x}{\mu} \right) d\mu . \tag{4.6}$$

Integration of equation (4.5) over frequency yields the total power per electron

$$\bar{P} = \frac{4e^4 \psi^2 B^2}{9 m_e^2 c^3} \qquad (\propto \text{ergs s}^{-1}) , \tag{4.7}$$

in agreement with equation (2.9) for the momentum loss rate $\langle \dot{p} \rangle_{\rm synch}$.

4.2. *High-Energy Cutoff*

We demonstrated in § 2 that when the momentum loss rate satisfies equation (4.1), every particle in a spherically symmetric accretion flow is driven towards the *critical Lorentz factor* (eq. [2.17])

$$\psi_c = 8.37 \times 10^4 (2 - \alpha) \left(\frac{B_0}{1\ \mu\text{G}} \right)^{-2} \left(\frac{|v_0|}{100\ \text{km s}^{-1}} \right) \left(\frac{r_0}{10\ \text{kpc}} \right)^{-1} \tag{4.8}$$

due to the combined influence of Fermi acceleration and synchrotron losses. Hence particles injected into an accretion flow with Lorentz factor ψ_0 are subsequently confined to the range (ψ_0, ψ_c), and the high-energy distribution function truncates at $\psi_{\max} \equiv \text{Max}(\psi_0, \psi_c)$.

The characteristic frequency of the synchrotron radiation emitted by an isotropic distribution of relativistic electrons with Lorentz factor ψ is

$$\bar{\nu}_c = \frac{3\psi^2 eB}{16 m_e c} = 3.30 \times 10^6 B\psi^2 \text{ Hz} , \tag{4.9}$$

obtained by averaging equation (6.17c) of Rybicki & Lightman (1979) over pitch angle. If the electrons are injected with Lorentz factor ψ_0, then the highest frequency radiation is produced by electrons with $\psi = \text{Max}(\psi_0, \psi_c)$, and the radiation spectrum cuts off exponentially above

$$\nu_{\max} = 3.30\left(\frac{B}{1\ \mu\text{G}}\right) \text{Max}(\psi_0^2, \psi_c^2) \text{ Hz} , \tag{4.10}$$

which is a function of radius in general since we have assumed that $B^2 \propto v/r \propto r^{-1-\alpha}$. Hence if the electron distribution were homogeneous out to some maximum radius R, then the apparent size $D < R$ of the radio source would vary with frequency as $D \propto \nu^{-2/(1+\alpha)}$, or $D \propto \nu^{-1}$ for $\alpha = 1$.

4.3. *Radiation Spectrum*

The total volume emissivity ϵ_ν associated with the relativistic electron distribution f is

$$\epsilon_\nu = 4\pi\sqrt{3}\, e^3 m_e^2 c B \int_0^\infty \psi^2 W\left(\frac{\nu}{\psi^2 \nu_s}\right) f\, d\psi \qquad (\propto \text{ergs s}^{-1}\text{ cm}^{-3}\text{ Hz}^{-1}) , \tag{4.11}$$

where $W(x)$ is given by equation (4.6). It is straightforward to show that for a power-law electron distribution f, the spectral index $\alpha_R \equiv -\partial \ln \epsilon_\nu / \partial \ln \nu$ of the associated synchrotron emissivity is constant with $2\alpha_R + 3 = -\partial \ln f / \partial \ln \psi$ (e.g., Rybicki & Lightman 1979). We demonstrated in § 3 that for the case of momentum-independent diffusion, the steady state particle distribution resulting from monoenergetic or power-law electron injection resembles a power-law over a limited range of ψ. It follows that over a limited frequency range,

$$\alpha_R = \begin{cases} -3\eta/2 , & \text{monoenergetic } (\eta < 0) , \\ (3\eta - 3)/2 , & \text{monoenergetic } (\eta > 0) , \\ (L-3)/2 , & \text{power-law } (L \geq 4) . \end{cases} \tag{4.12}$$

We can calculate the synchrotron emissivity resulting from monoenergetic or power-law electron injection for the case of momentum-independent diffusion by substituting our expressions for f_G (eq. [3.6]) or f_S (eq. [3.28]) into equation (4.11). In keeping with the approach taken in § 3, we shall develop results for both positive and negative values of η.

4.3.1. *Monoenergetic Injection*

In Figures 10 and 11 we plot the self-consistent synchrotron emissivity radiated by electrons distributed according to the Green's functions in Figures 2 and 3, respectively, which describe the acceleration and momentum-independent diffusion of electrons injected monoenergetically into a cooling flow with $\psi_0 = 100$, $\alpha = 1$, $r_0 = 3 \times 10^{22}$ cm, $v_0 = -350$ km s^{-1}, $\dot{N}_0 = 10^{47}$ s^{-1}, and $\eta = -2$ (Fig. 10), $\eta = 2$ (Fig. 11). The injection radius $r_0 \sim 10$ kpc, which is comparable to the magnetic field reconnection radius (Soker & Sarazin 1990). Results are presented for $B_0 = 2.0\ \mu$G (*solid line*) and $B_0 = 6.5\ \mu$G (*dotted line*); the corresponding values of the critical Lorentz factor (eq. [2.17]) are $\psi_c = 7.52 \times 10^4$ and $\psi_c = 7.12 \times 10^3$, respectively. Since we have chosen fixed values for r_0, v_0, α, and $|\eta|$, the value of ξ_0 is determined by K_0, with $K_0 = 1.75 \times 10^{29}$ cm^2 s^{-1} ($\xi_0 = 3$) in Figure 10*a*, $K_0 = 5.25 \times 10^{30}$ cm^2 s^{-1} ($\xi_0 = 0.1$) in Figure 10*b*, $K_0 = 1.75 \times 10^{29}$ cm^2 s^{-1} ($\xi_0 = 3$) in Figure 11*a*, and $K_0 = 1.75 \times 10^{30}$ cm^2 s^{-1} ($\xi_0 = 0.3$) in Figure 11*b*.

As we discussed in § 3, decreasing K_0 increases the level of trapping throughout the flow, with consequences that depend markedly on the sign of η. For example, the emissivity curves in Figure 10*a* lie above the corresponding curves in Figure 10*b* because decreasing K_0 results in an increase in the electron density when $\eta < 0$ and $\xi_0 \lesssim 1$ (this effect can also be seen in the Green's function plots of Fig. 2). The behavior is similar when $\eta > 0$, except at large radii, where decreasing K_0 dramatically reduces both the electron density and the level of synchrotron emission (see Fig. 3). In Figures 10 and 11, the emissivity has a power-law shape over several decades in frequency with $\alpha_R = 3$ (Fig. 10), $\alpha_R = 1.5$ (Fig. 11), in agreement with equation (4.12). The spectra in Figures 10 and 11 begin to steepen significantly around the frequency $\nu_{\max} \sim 10^6 B\psi_c^2 \propto B_0^{-3}$ (eq. [4.10]). Consequently the emissivity curves for $B_0 = 2.0\ \mu$G extend roughly 1.5 orders of magnitude further in frequency than the corresponding curves for $B_0 = 6.5\ \mu$G. At low frequencies the spectra begin to flatten due to the low-energy cutoff in the electron distribution at $\psi = \psi_0$. The flattening is most pronounced at small radii where the magnetic field is strongest.

Previous treatments of electron diffusion in astrophysical radio sources (e.g., Wilson 1975) have generally neglected effects related to bulk motions of the background plasma. In our spherically symmetric model, the importance of bulk motions depends on the magnitude of the injection-radius flow velocity v_0. We examined the response of the Green's function to variations in v_0 in § 3 (Fig. 7) for cases involving the monoenergetic injection of electrons into a cooling flow with $\alpha = 1$, $\psi_0 = 100$, $r_0 = 3 \times 10^{22}$ cm, $\dot{N}_0 = 10^{47}$ s^{-1}, $B_0 = 6.5\ \mu$G, $K_0 = 1.75 \times 10^{29}$ cm^2 s^{-1}, and $\eta = \pm 2$. In Figure 12 we plot the self-consistent synchrotron emissivity radiated

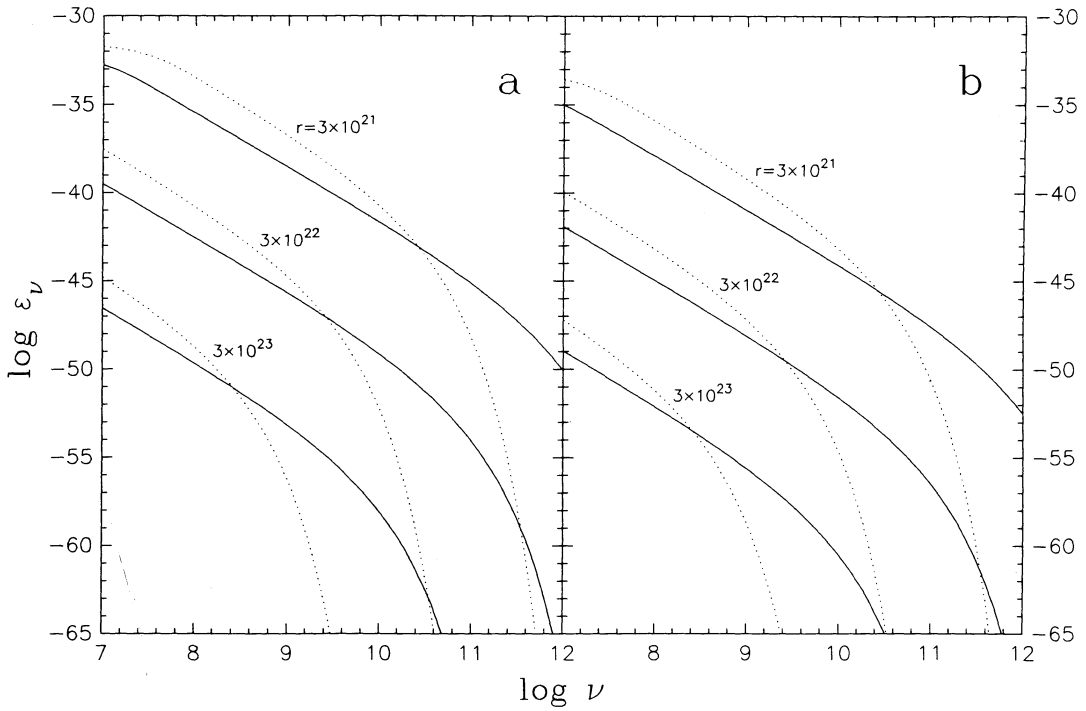

FIG. 10.—Self-consistent synchrotron emissivity ϵ_ν (eq. [4.11]) plotted (cgs units) as a function of frequency ν for electrons injected monoenergetically into a cooling flow with $\psi_0 = 100$, $\alpha = 1$, $r_0 = 3 \times 10^{22}$ cm, $v_0 = -350$ km s^{-1}, $\dot{N}_0 = 10^{47}$ s^{-1}, $\eta = -2$, and (*a*) $K_0 = 1.75 \times 10^{29}$ cm^2 s^{-1}, (*b*) $K_0 = 5.25 \times 10^{30}$ cm^2 s^{-1}. Results are presented for $B_0 = 2.0$ μG (*solid line*) and $B_0 = 6.5$ μG (*dotted line*). The emissivity curves were generated using the Green's functions plotted in Fig. 2. The radius (cm) is indicated for each curve.

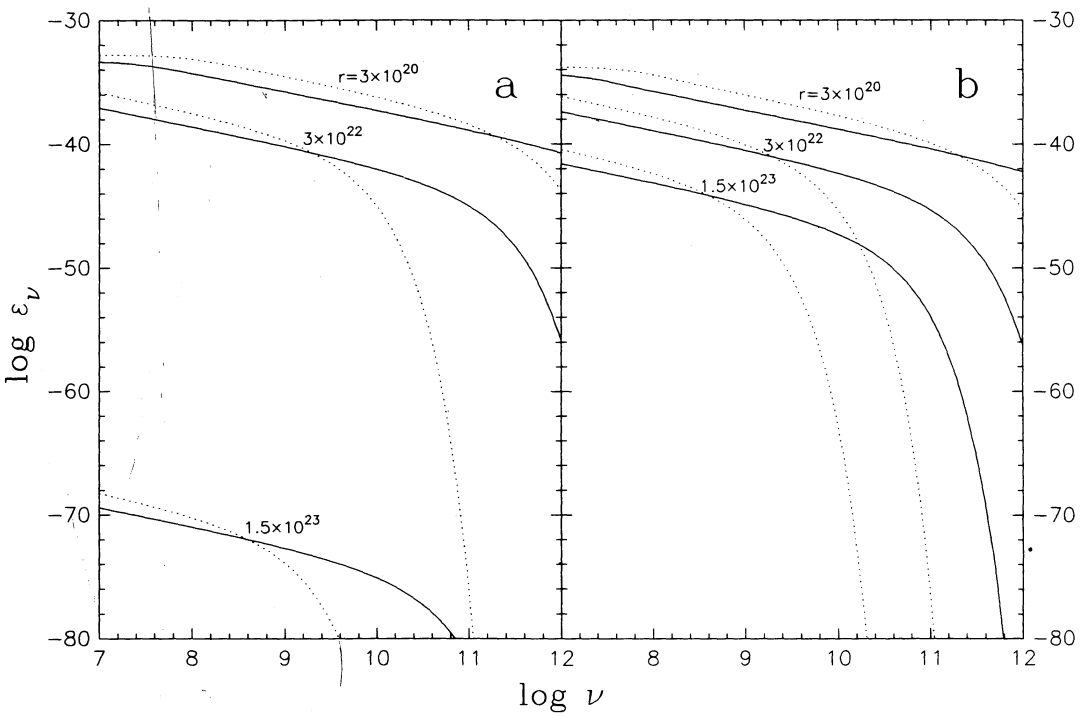

FIG. 11.—Same as Fig. 10, except $\eta = 2$ and (*a*) $K_0 = 1.75 \times 10^{29}$ cm^2 s^{-1}, (*b*) $K_0 = 1.75 \times 10^{30}$ cm^2 s^{-1}. The emissivity curves were generated by substituting the Green's functions plotted in Fig. 3 into eq. (4.11).

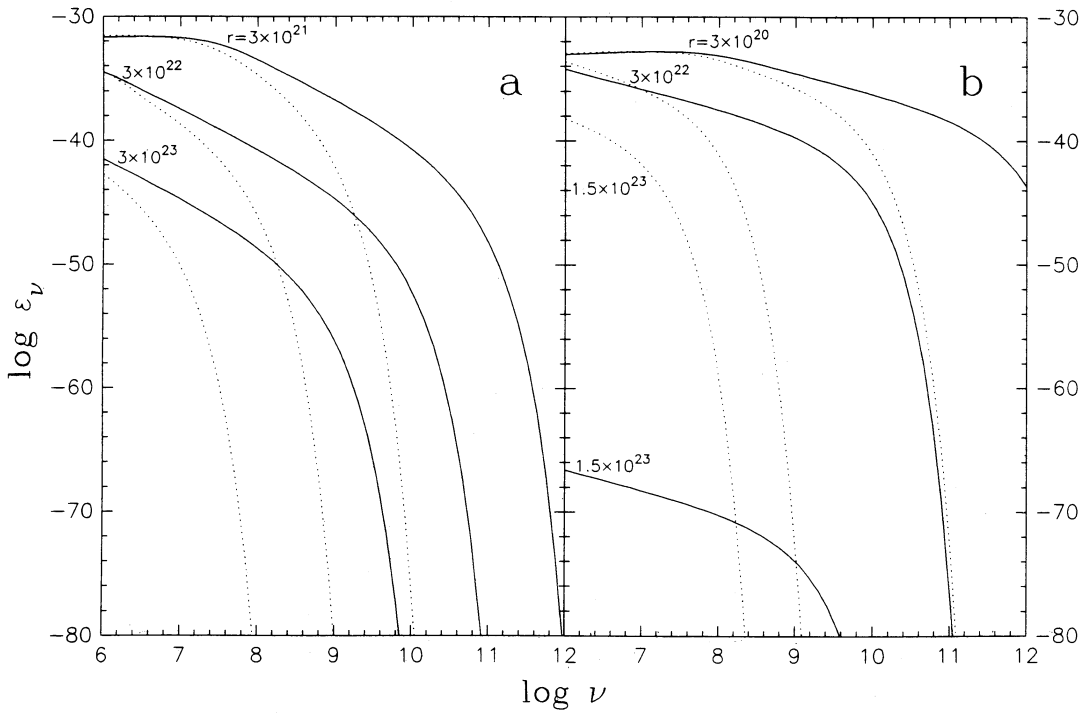

FIG. 12.—Self-consistent synchrotron emissivity ϵ_ν (eq. [4.11]) plotted (cgs units) as a function of frequency ν for electrons injected monoenergetically into a cooling flow with $\psi_0 = 100$, $\alpha = 1$, $r_0 = 3 \times 10^{22}$ cm, $B_0 = 6.5$ μG, $\dot{N}_0 = 10^{47}$ s^{-1}, $K_0 = 1.75 \times 10^{29}$ cm^2 s^{-1}, and (*a*) $\eta = -2$, (*b*) $\eta = 2$. Results are presented for $v_0 = -35$ km s^{-1} (*dotted line*) and $v_0 = -350$ km s^{-1} (*solid line*). The emissivity curves were generated using the Green's functions plotted in Fig. 7. The radius (cm) is indicated for each curve.

by electrons distributed according to the Green's functions in Figure 7, with $\eta = -2$ (Fig. 12*a*), $\eta = 2$ (Fig. 12*b*). Results are presented for $v_0 = -35$ km s^{-1} (*dotted line*) and $v_0 = -350$ km s^{-1} (*solid line*); the corresponding values of the critical Lorentz factor are $\psi_c = 7.12 \times 10^2$ and $\psi_c = 7.12 \times 10^3$, respectively.

In Figure 12*a*, each of the emissivity curves for $v_0 = -350$ km s^{-1} lies above the corresponding curve for $v_0 = -35$ km s^{-1} throughout essentially the entire plotted frequency range. Furthermore, the high-velocity curves extend roughly two decades further in frequency since $\nu_{\max} \sim 10^6 B \psi_c^2 \propto v_0^2$. The behavior is similar in Figure 12*b* except at large radii where the spatial attenuation is much more severe in the high-velocity case due to the positive value of η. In the zero-velocity limit, $\psi_c \ll \psi_0$, and therefore $\nu_{\max} \sim 10^6 B \psi_0^2$ according to equation (4.10). Since $(\psi_c/\psi_0)^2 \sim 5000$ for the $v_0 = -350$ km s^{-1} curves in Figure 12, we see that first-order Fermi acceleration has increased the maximum frequency of the radio emission by nearly four orders of magnitude.

4.3.2. *Power-Law Injection*

In Figures 13 and 14 we plot the self-consistent synchrotron emissivity for the steady-state electron distributions in Figures 8 and 9, respectively, which describe the acceleration and momentum-independent diffusion of electrons injected with a power-law spread in momentum into a cooling flow with $\alpha = 1$, $r_0 = 3 \times 10^{22}$ cm, $v_0 = -350$ km s^{-1}, $K_0 = 1.4 \times 10^{29}$ cm^2 s^{-1} ($\xi_0 = 3$), $D_0 = 10^{32}$ ergs^{-3} s^{-4}, and $\eta = -2.5$ (Fig. 13), $\eta = 2.5$ (Fig. 14). The injected power-law index $L = 5$ in Figures 13*a* and 14*a*, while $L = 6$ in Figures 13*b* and 14*b*. Results are presented for $B_0 = 2.0$ μG (*solid line*) and $B_0 = 6.5$ μG (*dotted line*); the corresponding values of the critical Lorentz factor are $\psi_c = 7.52 \times 10^4$ and $\psi_c = 7.12 \times 10^3$, respectively. In Figures 13 and 14, the emissivity has a power-law shape up to the cutoff frequency $\nu_{\max} \sim 10^6 B \psi_c^2$, with $\alpha_R = 1$ for $L = 5$ and $\alpha_R = 1.5$ for $L = 6$, in agreement with equation (4.12).

4.4. *Observational Diagnostics*

In order to predict the detailed appearance of a model core-halo embedded in a cooling flow, we must calculate the specific radio intensity by integrating the synchrotron emissivity ϵ_ν along lines of sight through the cluster. However, it is not our intention to produce definitive models of individual sources here, and we defer such calculations to future studies. Instead, we shall discuss the general implications of our theory for the production of amorphous radio emission in cooling flows, and attempt to estimate the most important theoretical parameters using observations of the spectral index and surface brightness reported by Gisler & Miley (1979) and by Miley & Perola (1975) for the core-halo surrounding NGC 1275 in the Perseus cluster.

Relativistic electrons injected at radius r_0 into a cooling flow with $\alpha = 1$ (i.e., $B \propto v \propto r^{-1}$) must diffuse "upstream" in order to produce extended radio emission on larger spatial scales. In our model, the number of electrons able to penetrate the outer region depends sensitively on the parameters η and ξ_0. The value of ξ_0 determines the relative importance of advection and diffusion at the injection radius, with $\xi_0 \gtrsim 1$ indicating significant particle trapping. In § 3 (Tables 2A and 3A), we noted that the total synchrotron luminosity is maximized for $\xi_0 \sim 1$. Since core halos are not particularly bright as a class, it is therefore likely that $\xi_0 \sim 1$ in the few that have been discovered, and we make that assumption in the following discussion. The sign of η determines whether the electrons

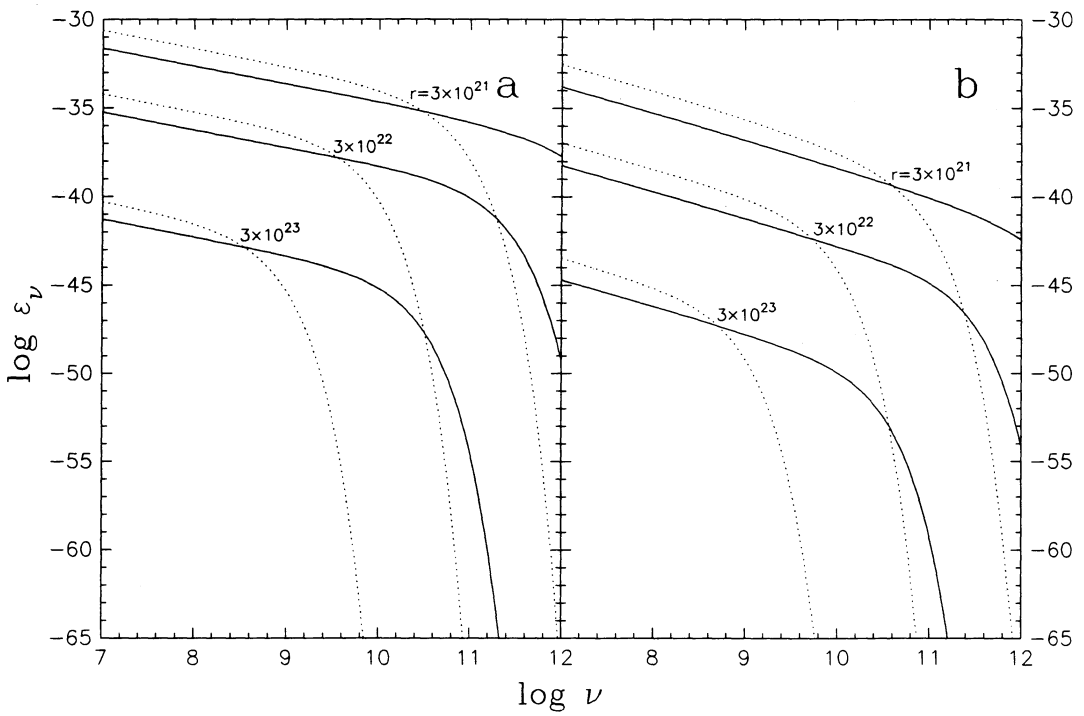

FIG. 13.—Self-consistent synchrotron emissivity ϵ_ν (eq. [4.11]) plotted (cgs units) as a function of frequency ν for electrons injected with a power-law spread in momentum into a cooling flow with $\alpha = 1$, $r_0 = 3 \times 10^{22}$ cm, $v_0 = -350$ km s^{-1}, $D_0 = 10^{32}$ ergs^{-3} s^{-4}, $K_0 = 1.4 \times 10^{29}$ cm^2 s^{-1}, $\eta = -2.5$, and (*a*) $L = 5$, (*b*) $L = 6$. Results are presented for $B_0 = 2.0$ μG (*solid line*) and $B_0 = 6.5$ μG (*dotted line*). The emissivity curves were generated using the Green's functions plotted in Fig. 8. The radius (cm) is indicated for each curve.

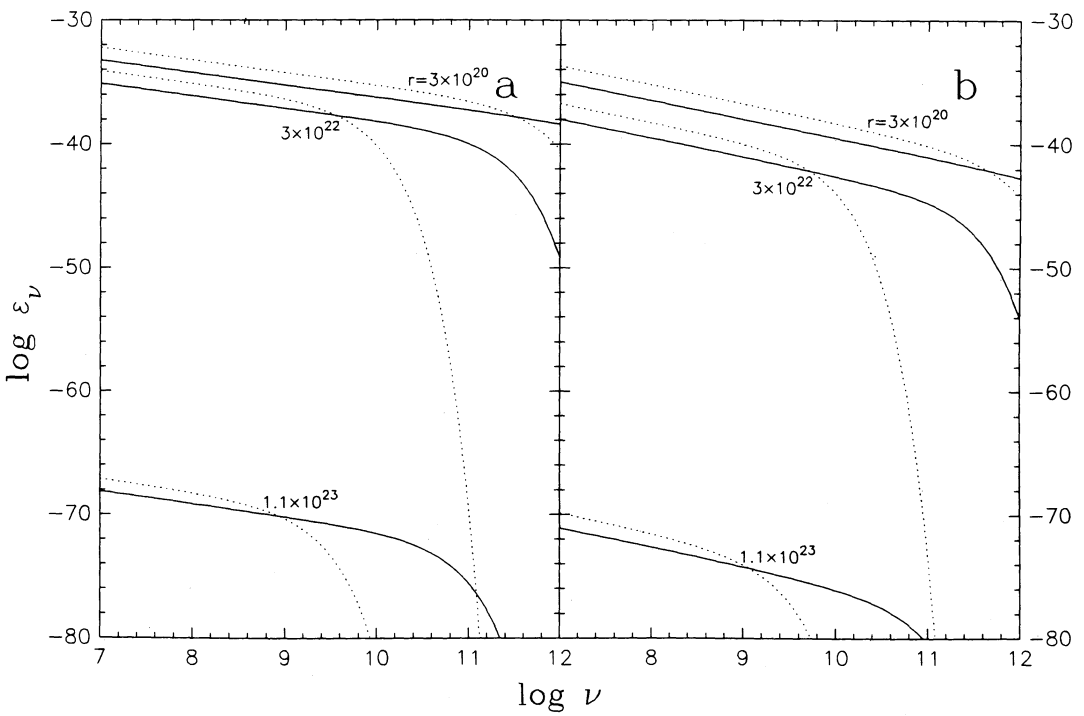

FIG. 14.—Same as Fig. 13, except $\eta = 2.5$. The emissivity curves were generated by substituting the Green's functions plotted in Fig. 9 into eq. (4.11).

become more ($\eta > 0$) or less ($\eta < 0$) trapped with increasing radius. When $\eta < 0$, the electron number density n varies as a power-law in radius throughout the flow; when $\eta > 0$, the power-law behavior is preserved at small radii ($r \ll r_0$), but n decays exponentially as $r \to \infty$. The sign of η is therefore expected to have a profound effect on the variation of the specific radio intensity I_ν: if $\eta < 0$, then I_ν will fade smoothly with increasing radius, and the apparent size D of the radio source will vary with frequency as $D \propto \nu^{-1}$ according to equation (4.10); if $\eta > 0$, then I_ν will drop drastically in the outer region ($r > r_0$) due to the dearth of electrons (since we have assumed that $\xi_0 \sim 1$), and $D \sim r_0$ for all $\nu \lesssim 10^6 B_0 \psi_{\max}^2$, where B_0 denotes the magnetic field strength at the injection radius and $\psi_{\max} \equiv \text{Max}\,(\psi_0, \psi_c)$. In any event, the apparent size can never exceed the cooling radius (obtained by setting the cooling time equal to the Hubble time), which defines the edge of the cooling flow.

In our model, the value of η is directly related to the derivative of the specific intensity I_ν with respect to the radius r. In particular, asymptotic analysis of equation (3.12b) for the differential synchrotron power indicates that for $\alpha_R \equiv -\partial \ln \epsilon_\nu / \partial \ln \nu = \text{constant}$,

$$\frac{\partial \ln I_\nu}{\partial \ln r} \approx \eta - 1 - \alpha_R \tag{4.13}$$

towards the center of the radio halo for $\eta > 0$, or towards the limb for $\eta < 0$. In deriving this result, we have assumed that $\alpha_R > \eta - 1$ (intensity increases toward the center) and that $\alpha_R > 1$ (most of the energy radiated at low frequencies). We have also assumed that the synchrotron emission is optically thin. Using equation (4.13), a measurement of $\partial \ln I_\nu / \partial \ln r$ near the center ($\eta > 0$) or the edge ($\eta < 0$) of the radio halo could be used to constrain η and α_R. The sign of η can be determined independently by examining the rate of limb-darkening and the variation of the source size with observing frequency.

For a fixed observing frequency ν_*, the slope of the observed radio spectrum will vary with radius in a manner that reflects the shape of the underlying electron energy distribution as follows: (i) The intensity $I_\nu(\nu_*)$ will appear to steepen at radius $r_{\text{steep}} \sim 10^6 B_0 r_0 \psi_{\max}^2 / \nu_*$ due to the high-energy cutoff in the electron distribution at $\psi_{\max} \equiv \text{Max}\,(\psi_0, \psi_c)$, with $I_\nu(\nu_*)$ dropping sharply for $r > r_{\text{steep}}$. If $\eta > 0$ and $r_{\text{steep}} \gtrsim r_0$, then the steepening at frequency ν_* will be unobservable due to the spatial attenuation of the electron distribution. (ii) For $r < r_{\text{steep}}$, $I_\nu(\nu_*) \propto \nu_*^{-\alpha_R}$, with the value of α_R (eq. [4.12]) determined by the power-law index of the electron distribution. (iii) If the electron distribution has a low-energy cutoff at $\psi = \psi_{\min}$, then $I_\nu(\nu_*)$ will appear to flatten at radius $r_{\text{flat}} \sim 10^6 B_0 r_0 \psi_{\min}^2 / \nu_*$. Hence our model generally predicts that the spectral index will increase with increasing radius.

4.5. *Interpretation of Radio Observations*

Gisler & Miley (1979) observed the Perseus cluster (A426) at 610 and 1415 MHz and found that the flux at both frequencies ends abruptly at the same radius, ~ 100 kpc, without fading smoothly into the noise. This radius is comparable to the cooling radius calculated for the Perseus cluster by Arnaud (1988) using *Einstein* HRI data, suggesting that the sharp truncation of the surface brightness is due to the finite size of the cooling flow. Using their data, Gisler and Miley derived the distribution of the spectral index α_R for the central 5′ of the cluster. The procedure they used involves the subtraction of an unresolved flat-spectrum component located near the center of the radio halo, which introduces unknown errors in the spectral index distribution. Their Figure 6 indicates that the distribution obtained is complex and asymmetric, with α_R tending to increase from 0.6 to 1.6 as $r \to 0$ in the cluster. In our model, α_R *decreases* with decreasing radius, culminating in a flat-spectrum core if the electron distribution has a low-energy cutoff. However, this discrepancy is not surprising since the predicted flat-spectrum component would have been removed in the data analysis procedure. We point out that a spectral index distribution of the expected form has been observed in the cooling-flow cluster PKS 0745−191 (Baum & O'Dea 1991).

In order to use the Gisler and Miley data to constrain the theoretical parameters without becoming mired in technical details regarding source calibration, we shall focus on the behavior of the spectral index in the northern section of the radio halo, where α_R decreases from 1.6 to 1 as $r \to 0$. If we assume that the steepening of the radio spectrum in the north reflects the fact that $\nu_{\max} \sim 1.4$ GHz at the limb, then observations at smaller radii should reveal the canonical value of α_R associated with the underlying power-law electron distribution. With α_R determined, measurement of $\partial \ln I_\nu / \partial \ln r$ would allow the calculation of η using equation (4.13). Analysis of the two lowest flux curves in the 1415 MHz contour map published by Miley & Perola (1975) yields $\partial \ln I_\nu / \partial \ln r \sim -4$ near the northern edge of the Perseus halo. Taking the limiting value $\alpha_R \sim 1$ then yields $\eta \sim -2$. Hence a power-law injection model with $\alpha = 1$, $v_0 = -350$ km s^{-1}, $\eta = -2$, $\xi_0 = 1$, and $L = 5$ may be consistent with the data, although this must be considered a crude estimate due to the uncertainties in the spectral index distribution. The observations of GHz radio emission ~ 100 kpc from the cluster center require $B_0 \sim 3.1$ μG, which is consistent with the magnetic field data (Sarazin 1986). We conclude by pointing out that the values of the luminosity in Tables 2 and 3 obtained using parameters thought to be relevant for galaxy cluster cooling flows lie within the observed range of core-halo radio luminosities (Hanisch 1982).

5. DISCUSSION

In this paper we have examined the steady state transport of relativistic particles expelled by a source located at a fixed radius in a spherical background flow of scatterers. The model incorporates the effects of spatial diffusion, first-order Fermi acceleration, bulk advection, and losses proportional to the square of the particle momentum, assuming power-law forms for the flow velocity and for the spatial dependence of the diffusion coefficient. We find that bulk motions play a dual role in controlling both the spatial transport and the energization of the relativistic particles diffusing through the background plasma. Bulk motions dominate the spatial transport when the advected particle flux exceeds that due to diffusion, with the transition between diffusion-dominated and advection-dominated behavior occurring at the trapping radius r_t (eq. [2.42]). Bulk motions dominate the particle energetics when the first-order Fermi acceleration rate exceeds the momentum loss rate, with the transition between acceleration-dominated and loss-dominated behavior occurring at the critical Lorentz factor ψ_c (eq. [2.17]). Previous studies of particle acceleration in accretion flows (e.g., Gleeson & Webb 1980) lacked self-consistent treatments of synchrotron and inverse-Compton losses. Conversely,

previous studies of electron diffusion in astrophysical radio sources (e.g., Wilson 1975) generally neglected effects related to bulk motions of the background plasma. Since advection, diffusion, acceleration, and losses are all likely to play a role in producing extended radio emission in cooling flows, we have been motivated to reexamine the general problem of particle transport in dynamic media.

In § 2 we derived the Green's function for cases with ψ_c = constant, implying that particles injected with Lorentz factor ψ_0 are confined to the interval (ψ_0, ψ_c) throughout the flow. The behavior of this solution was examined in detail in § 3 for the case of momentum-independent diffusion, and closed-form expressions were obtained for the number and energy densities of the relativistic particles, and for the steady state particle distribution resulting from the continual injection of particles with a power-law spread in momentum. Our theory can be used to model relativistic particle transport in a variety of astrophysical environments. As an application, in § 4 we considered in detail the acceleration of electrons in galaxy-cluster cooling flows, and explored the consequences of our model for the production of core-halo radio emission. In these cooling-flow cases, we assumed that the injection occurs at $r_0 = 3 \times 10^{22}$ cm, which is consistent with the reconnection radius (~ 10 kpc) derived by Soker & Sarazin (1990). The injection-radius flow velocity and the injection-radius magnetic field were generally set at $v_0 = -350$ km s^{-1} and $B_0 = 6.5$ μG, respectively, and several values for the injection-radius diffusion coefficient were selected in the range $K_0 \sim 10^{29-31}$ cm^2 s^{-1}, yielding marginal trapping at r_0. Note that the background flow in our model is both subsonic and sub-Alfvénic for the temperatures $\sim 10^{7-8}$ K and densities $\sim 10^{-3}$ cm^{-3} typical of cooling flows. Our assumption of marginal trapping at the injection radius ensures that the diffusion velocity also satisfies these constraints. Parallel results were developed for positive and negative values of η (eq. [2.27]), yielding trapping-dominated behavior at large and small radii, respectively. In § 4 we also discussed the utilization of the observed surface brightness and spectral index distributions to constrain the theoretical parameters, using the Perseus core-halo as an example.

The assumption ψ_c = constant is probably justified in cooling flows, since theoretical models suggest that $B \propto v \propto r^{-1}$ (Soker & Sarazin 1990; White & Sarazin 1987). We wish to emphasize that: (i) our model can easily produce core-halo radio emission in the observed luminosity range for reasonable values of the cluster magnetic field strength and flow velocity; (ii) observable fluxes of synchrotron radiation can be emitted even when the relativistic electrons are unable to escape from the inflow due to strong trapping at large radii, which occurs for positive values of η; (iii) power-law radio spectra can be produced as a result of either monoenergetic or power-law electron injection; and (iv) first-order Fermi acceleration can extend the maximum frequency of the radio emission in cooling flows several orders of magnitude beyond the cutoff associated with static diffusion models.

If core halos with radii ~ 100 kpc are produced as a consequence of Fermi acceleration in cooling flows, then the amorphous radio emission provides independent observational evidence for the dynamical nature of the cooling process in clusters of galaxies. Larger halos with radii ~ 1 Mpc occur in Coma and other relaxed clusters which generally lack central-dominant galaxies and cooling flows, but which often possess at least two giant ellipticals, suggesting recent mergers (Fabian, Nulsen, & Canizares 1984; Stewart et al. 1984). The size of the Coma halo necessitates in situ reacceleration if the electrons powering the radio emission originated at the cluster center (Jaffe 1977). If the rarity of Coma-class halos reflects the requirement of recent merger activity, then it may be worth examining merger-driven turbulence as a possible reacceleration mechanism. In this view, Coma-class halos may represent a temporary evolutionary phase during which subcluster mergers drive turbulence at a level sufficient to (i) disrupt the existing cooling flow and (ii) reaccelerate the electrons diffusing outward from the center. Cooling flows and Coma-class radio halos may even coexist briefly during the period between merger and cooling-flow disruption; A2319 may be an example of this phenomenon (Sarazin 1986; Vestrand 1982).

Roland (1981) has investigated the amplification of intracluster magnetic fields via MHD turbulence in galaxy wakes and finds that the field grows until the Alfvén velocity $v_A = B/\sqrt{4\pi\rho}$ becomes equal to the turbulent velocity v_t. Jaffe (1977) has considered second-order Fermi acceleration due to turbulent eddies with velocity $v_t = v_A$ as the energy source in models of the Coma halo. He concludes that the dissipated power implied by the radio observations exceeds the X-ray luminosity $L_x \sim 10^{44-45}$ ergs s^{-1} by roughly four orders of magnitude. However, if the typical eddy size is equal to the dominant Alfvén wavelength r_A as expected for MHD turbulence, then Jaffe's result requires that essentially all of the magnetic energy $B^2/(8\pi)$ be dissipated in one Alfvén time $t_A = r_A/v_A$, while detailed calculations suggest that the timescale for dissipating the energy contained in the *turbulent* component of the magnetic field B_t is $(B/B_t)^2 t_A \gg t_A$ (e.g., Benford, Ferrari, & Trussoni 1980). Therefore the effective time scale for dissipating *all* of the magnetic energy is $\tau^{-4} t_A$, where $\tau \equiv B_t/B$. Setting $\tau = 0.1$ increases Jaffe's estimate of the dissipation time scale by four orders of magnitude, which brings the dissipated power into agreement with the X-ray observations. Since X-ray luminosities in the range $L_x \sim 10^{44-45}$ ergs s^{-1} are typical of cooling flows, we see that the damping of merger-driven Alfvénic turbulence can provide enough energy to disrupt an existing cooling flow and explain the production of the extended X-ray and radio emission.

We have not attempted to realistically model the cooling cores here, or to address the relationship between the X-ray and radio emitting plasmas, except to say that the core-halo radius should always be smaller than the cooling radius (~ 100 kpc) since the relativistic electrons are confined and accelerated by magnetic scattering centers (i.e., Alfvén waves) converging with the thermal plasma. While the canonical values we have chosen for the flow velocity, the diffusion coefficient, the magnetic field, and the injection radius are all reasonable for cooling flows, we have neglected inverse-Compton losses, which swamp synchrotron losses whenever $B \lesssim 3$ μG. The inclusion of inverse-Compton losses is not expected to significantly modify the specific results we have obtained for cooling flows with $B_0 = 6.5$ μG, since most of the radio emission comes from radii $r \lesssim 2r_0$ where $B \gtrsim 3$ μG. However, observations of the Perseus core-halo may require $B_0 \sim 3.1$ μG (see § 4), and in order to treat this case in detail inverse-Compton losses would therefore have to be included. Two other outstanding issues concern the distribution of particle sources within the cluster and the momentum dependence of the diffusion coefficient, which affect the size and the flux distribution of the amorphous radio emission. Although our formalism can accommodate distributed injection and momentum-dependent diffusion, in most of the numerical examples presented here, we have assumed for simplicity that the diffusion coefficient is independent of the particle momentum and that the electrons are injected from a shell source located at radius r_0. In fact, the electrons may be expelled by a

single active galaxy located at the cluster center or they may be produced by active galaxies distributed throughout the cluster core, and the radial and momentum dependences of the diffusion coefficient should be computed using the correct MHD expressions. We plan to consider the effects of distributed injection and momentum-dependent diffusion in future calculations. We also intend to treat momentum diffusion (statistical acceleration) and supercritical power-law injection (i.e., $\psi_0 > \psi_c$), and to produce simulated intensity distributions for specific sources.

I am grateful to Steve Balbus for suggesting this research topic, and to him and the Astronomy Department at the University of Virginia for support during the early part of the work. I also acknowledge support from the National Research Council and the Naval Research Laboratory.

APPENDIX

In this section we use Laplace transform techniques to derive the steady state distribution function describing the transport of electrons injected monoenergetically by a source at radius r_0. The particle transport is governed by the equation

$$\frac{\partial g}{\partial x} = \frac{\partial}{\partial y}\left(y^{2-\eta}\frac{\partial g}{\partial y}\right) + \frac{3\dot{N}_0}{(4\pi r_0)^2 m_e^3 c^3 |v_0|}\delta(x)\delta(y - y_0)\,, \tag{A1}$$

derived in § 2. Operating on equation (A1) with $\int_0^\infty e^{-sx}dx$ yields

$$sG(s, y) - \frac{\partial}{\partial y}\left(y^{2-\eta}\frac{\partial G}{\partial y}\right) = \frac{3\dot{N}_0}{(4\pi r_0)^2 m_e^3 c^3 |v_0|}\delta(y - y_0)\,, \tag{A2}$$

where

$$G(s, y, y_0) \equiv \int_0^\infty e^{-sx} g(x, y, y_0)dx \tag{A3}$$

denotes the Laplace transform of the function g with respect to x. The differential equation (A2) for G can be stated more simply in terms of the variables

$$a \equiv \frac{2\sqrt{s}}{|\eta|}\, y^{\eta/2}\,, \qquad b \equiv \frac{2\sqrt{s}}{|\eta|}\, y_0^{\eta/2}\,, \tag{A4}$$

and the function H, where

$$G(s, y, y_0) \equiv \frac{6\dot{N}_0 (y y_0)^{(\eta-1)/2}}{(4\pi r_0)^2 |\eta|\,|v_0|\, m_e^3 c^3} H(a, b)\,. \tag{A5}$$

After some algebra, equation (A2) reduces to

$$a^2 H'' + aH' - (\mu^2 + a^2)H = -b\delta(a - b)\,, \tag{A6}$$

where primes denote differentiation with respect to a, and

$$\mu \equiv 1 - \frac{1}{\eta}\,. \tag{A7}$$

We shall restrict our attention to the case $\mu > 0$, which corresponds to either $\eta < 0$ or $\eta > 1$. The solutions to equation (A6) are superpositions of the modified Bessel functions $I_\mu(a)$ and $K_\mu(a)$;

$$H(a, b) = \begin{cases} c_1 K_\mu(a) + c_2 I_\mu(a)\,, & |a| \le |b|\,, \\ d_1 K_\mu(a) + d_2 I_\mu(a)\,, & |a| \ge |b|\,. \end{cases} \tag{A8}$$

The delta function inhomogeneity in equation (A6) creates a finite jump in H' at the point $a = b$. To determine the magnitude of this jump, we integrate equation (A6) with respect to a over an infinitesimal region around $a = b$, yielding the condition

$$H'\Big|_{a=b-\epsilon}^{a=b+\epsilon} = -1/b\,. \tag{A9a}$$

The function H must also satisfy the continuity condition

$$H\Big|_{a=b-\epsilon}^{a=b+\epsilon} = 0\,. \tag{A9b}$$

We lose no generality by setting $c_1 = d_2 = 0$ in equation (A8), since the functions I_μ and K_μ each give convergent results for the inverse transformation

$$h(x, y, y_0) \equiv \frac{1}{2\pi i}\int_{\gamma-i\infty}^{\gamma+i\infty} e^{xs} H(s)ds\,, \tag{A10}$$

so long as the line Re $s = \gamma$ is chosen to lie to the right of any singularities in the integrand. Equations (A8) and (A9) can then be combined to obtain

$$c_2 = \frac{K_\mu(b)}{bW(b)} = K_\mu(b)\,, \qquad d_1 = \frac{I_\mu(b)}{bW(b)} = I_\mu(b)\,, \tag{A11}$$

where

$$W(a) \equiv K_\mu(a)I'_\mu(a) - I_\mu(a)K'_\mu(a) = 1/a \tag{A12}$$

denotes the Wronskian of the two solutions K_μ and I_μ (Abramowitz & Stegun 1970). The final result for H is

$$H(a, b) = \begin{cases} K_\mu(b)I_\mu(a)\,, & |a| \le |b|\,, \\ I_\mu(b)K_\mu(a)\,, & |a| \ge |b|\,. \end{cases} \tag{A13}$$

Our remaining task is to invert the transform by evaluating the complex integral in equation (A10). Although the integrand has no poles, we must take into account the branch point of the complex square root function located at the origin. In order to avoid the branch point, and the branch line extending to $s = -\infty$, we integrate along the closed contour shown in Figure 15. Since the function $e^{xs}H(s)$ is everywhere analytic, its integral over the contour vanishes according to the Cauchy theorem. As the radius R_1 of the arcs MN and QR increases without bound, the contribution to the integral from these arcs vanishes (see eqs. [9.7.1] and [9.7.2] of Abramowitz & Stegun 1970). Similarly, the integral around the small circle OP vanishes in the limit $R_2 \to 0$. Hence we need only evaluate the integral along the negative real semiaxis. On the segment NO, we have $s = re^{i\pi}$, and therefore $\sqrt{s} = i\sqrt{r}$. On the segment PQ, we have $s = re^{-i\pi}$, and therefore $\sqrt{s} = -i\sqrt{r}$. Combining these expressions with equations (A4), (A10), and (A13), we have

$$h(x, y, y_0) = \frac{1}{2\pi i}\int_0^\infty \left\{K_\mu\left[-\frac{2iy_0^{\eta/2}\sqrt{r}}{|\eta|}\right]I_\mu\left[-\frac{2iy^{\eta/2}\sqrt{r}}{|\eta|}\right] - K_\mu\left[\frac{2iy_0^{\eta/2}\sqrt{r}}{|\eta|}\right]I_\mu\left[\frac{2iy^{\eta/2}\sqrt{r}}{|\eta|}\right]\right\}e^{-xr}\,dr\,. \tag{A14}$$

Using relations between the various Bessel functions, we can rewrite this integral as

$$h(x, y, y_0) = \frac{1}{2}\int_0^\infty J_\mu\left[\frac{2y_0^{\eta/2}\sqrt{r}}{|\eta|}\right]J_\mu\left[\frac{2y^{\eta/2}\sqrt{r}}{|\eta|}\right]e^{-xr}dr\,, \tag{A15}$$

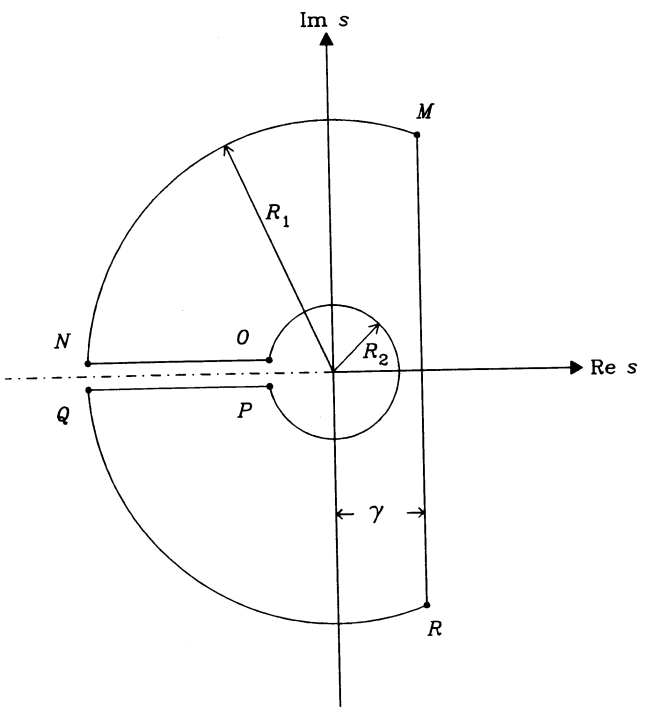

FIG. 15.—Contour used to perform the Laplace inversion integral in complex space (eq. [A10]). The dot-dashed line denotes the branch line of the complex square root function. In the limit $R_1 \to \infty$, $R_2 \to 0$, the integral along the segment RM can be replaced with an integral along the segments NO and PQ. The line Re $s = \gamma$ must lie to the right of any singularities in the integrand.

which can be evaluated using equation (6.615) of Gradshteyn & Ryzhik (1980) to obtain

$$h(x, y, y_0) = \frac{1}{2x} \exp\left[-\left(\frac{y_0^\eta + y^\eta}{\eta^2 x}\right)\right] I_\mu\left[\frac{2(yy_0)^{\eta/2}}{\eta^2 x}\right]. \quad \text{(A16)}$$

Combining this expression with equation (A5) yields the final result (Eichler 1979; Webb 1982)

$$g(x, y, y_0) = \frac{3\dot{N}_0}{(4\pi r_0)^2 m_e^3 c^3 |v_0|} \frac{(yy_0)^{(\eta-1)/2}}{|\eta| x} \exp\left[-\left(\frac{y_0^\eta + y^\eta}{\eta^2 x}\right)\right] I_\mu\left[\frac{2(yy_0)^{\eta/2}}{\eta^2 x}\right]. \quad \text{(A17)}$$

REFERENCES

Abramowitz, M., & Stegun, I. A. 1970, Handbook of Mathematical Functions (NY: Dover)
Arnaud, K. A. 1988, preprint
Baum, S. A., & O'Dea, C. P. 1991, MNRAS, 250, 737
Becker, P. A., & Begelman, M. C. 1986, ApJ, 310, 534
Benford, G., Ferrari, A., & Trussoni, E. 1980, ApJ, 241, 98
Begelman, M. C. 1979, MNRAS, 187, 237
———. 1986, Nature, 322, 614
Burns, J. O. 1990, AJ, 99, 14
Cowsik, R. 1986, A&A, 155, 344
Cowsik, R., & Lee, M. A. 1982, Proc. Roy. Soc. Lond., 383, 409
De Young, D. S. 1980, ApJ, 241, 81
Eichler, D. 1979, ApJ, 229, 409
Eilek, J. A. 1984, in Physics of Energy Transport in Extragalactic Radio Sources, ed. A. H. Bridle & J. A. Eilek (Green Bank, WV: NRAO), 216
Erdélyi, A., Magnus, W., Oberhettinger, F., & Tricomi, F. G. 1954, Tables of Integral Transforms (NY: McGraw-Hill)
Fabian, A. C., Arnaud, K. A., Nulsen, P. E. J., & Mushotzky, R. F. 1986, ApJ, 305, 9
Fabian, A. C., Nulsen, P. E. J., & Canizares, C. R. 1984, Nature, 310, 733
Gisler, G. R., & Miley, G. K. 1979, A&A, 76, 109
Gleeson, L. J., & Axford, W. I. 1967, ApJ, 149, L115
Gleeson, L. J., & Webb, G. M. 1978, Ap&SS, 58, 21
———. 1980, Fund. Cosmic Phys., 6, 187
Gradshteyn, I. S., & Ryzhik, I. M. 1980, Table of Integrals, Series, and Products (NY: Academic)
Hanisch, R. J. 1982, A&A, 116, 137
Hanisch, R. J., & Erickson, W. C. 1980, AJ, 85, 183
Hennessy, G. S., Owen, F. N., & Eilek, J. A. 1989, ApJ, 347, 144
Jaffe, W. J. 1977, ApJ, 212, 1
———. 1980, ApJ, 241, 925
Jokipii, J. R. 1971, Phys. Rev. Lett., 26, 666
Kardashev, N. S. 1962, Soviet Astron., 6, 317
Kirk, J. G. 1987, private communication
Lerche, I., & Schlickeiser, R. 1988, Ap&SS, 145, 319
Miley, G. K., & Perola, G. C. 1975, A&A, 45, 223
Parker, E. N. 1965, Planet Space Sci., 13, 9
Payne, D. G., & Blandford, R. D. 1981, MNRAS, 196, 781
Roland, J. 1981, A&A, 93, 407
Rybicki, G. B., & Lightman, A. P. 1979, Radiative Processes in Astrophysics (NY: Wiley)
Sarazin, C. L. 1986, Rev. Mod. Phys., 58, 1
Schlickeiser, R. 1989a, ApJ, 336, 243
———. 1989b, ApJ, 336, 264
Schneider, P., & Bogdan, T. J. 1989, ApJ, 347, 496
Skilling, J. A. 1975, MNRAS, 172, 557
Soker, N., & Sarazin, C. L. 1990, ApJ, 348, 73
Stewart, G. C., Fabian, A. C., Jones, C., & Forman, W. 1984, ApJ, 285, 1
Vestrand, W. T. 1982, AJ, 87, 1266
Webb, G. M. 1982, Ap&SS, 81, 215
Webb, G. M., & Bogdan, T. J. 1987, ApJ, 320, 683
White, III, R. E., & Sarazin, C. L. 1987, ApJ, 318, 629
Wilson, A. S. 1975, A&A, 43, 1